Stony Brook University

Throat intersection in pore networks and application to reactive flow

A Dissertation Presented

by

Joo-won Kim

to

The Graduate School

in Partial Fulfillment of the

Requirements

for the Degree of

Doctor of Philosophy

in

Applied Mathematics and Statistics

(Computational Applied Mathematics)

Stony Brook University

May 2014

Stony Brook University

The Graduate School

Joo-won Kim

We, the dissertation committee for the above candidate for the

Doctor of Philosophy degree, hereby recommend

acceptance of this dissertation.

W. Brent Lindquist – Dissertation Advisor
Professor of Applied Mathematics and Statistics

Xiaolin Li - Chairperson of Defense
Professor of Applied Mathematics and Statistics

Xiangmin Jiao - Committee Member
Associate Professor of Applied Mathematics and Statistics

Keith Jones - Outside Member
Adjunct Professor of Material Science and Engineering

This dissertation is accepted by the Graduate School

Charles Taber
Dean of the Graduate School

Abstract of the Dissertation

Throat intersection in pore networks and application to reactive flow

by

Joo-won Kim

Doctor of Philosophy

in

Applied Mathematics and Statistics

(Computational Applied Mathematics)

Stony Brook University

2014

The concept of throats in porous media is critically re-examined as a geometric quantity with maintaining the standard notion of a throat as a locally minimum-area cross section in the void space. We demonstrate that throats can intersect each other. We show with flow simulation that these intersecting throats correspond to capillary pressure controlled entry points during drainage. We have developed a throat finding algorithm that explicitly allows and locates intersecting throats, using a planar approximation for robustness and speed. We show that the probability of intersecting throats increases significantly if the porosity is above 20%; in the sand pack, over 1/4 of all throats are intersecting throats. Using this pore network and other image analysis techniques, we analyze x-ray computed microtomography images of reactive flow experiments. Dissolution and re-precipitation are main reactions causing changes of pore structures and flow behavior. We especially observe intra dissolution as well as hollow grain produced by the combination of dissolution and precipitation. Comparing images of different

time stamp voxel by voxel after fine registration makes it possible to trace the phase change such as early dissolution, late dissolution, or dissolution followed by re-precipitation. The dissolution and precipitation depth layer shows how deeply the reaction influences as well as how differently intra and surface dissolution occur. The reactions dramatically change pore structures; intra dissolution produces new pores; surface dissolution enlarges pore size or merges pores; precipitation reduces pore size, splits pores or removes pores.

To my parents

Table of Contents

List of Figures

List of Tables

Acknowledgments

I would like to thank my advisor, Professor W. Brent Lindquist, for his guidance, advice, and support. I also thank my committee members, Professor Xiaolin Li, Professor Xiangmin Jiao, and Professor Keith Jones. My lab members and colleagues are always helpers. I thank Dr. Daesang Kim, Seunghee, Long, and Dr. Maša Prodanović.

Especially, I would like to thank my loving parents, Kwanyeol Kim and Byeongyeon Min for their love and support. I thank my sister, Jung-a, too. I also thank my friends, Jeewoen, Dr. Hyunkyung Lim, Hyungkeun, Dr. Jayon Lihm, Kwangmin, and Soyoun.

Chapter 1

Introduction

The pore scale image analysis of porous media has been performed since X-ray computed microtomography (XCMT) was developed[1-4]. This pore scale analysis advanced the research of multi-phase flow, contamination flow, carbon storage and enhanced oil recovery[5-7]. The up-scaling characterizes the core-level or field-level properties[8,9].

Throats play a fundamental role in the two-phase-flow drainage process: in the vadose zone (air-water) and in the saturated zone (where the two phase drainage process is, almost universally, organic-water with the organic phase being either liquid or gas)[10,11]. By extension, throats are equally important in three-phase flow. Throats also play a strong role in determining single phase conductivity[12]. Throats locally control the movement of the terminal menisci that define the invading fluid front and their shape plays a role in the formation of the arc menisci that define wetting films[13-18]. Pore-network models[19] are one of the main numerical tools used to model flow at the pore-scale. These models require increasingly accurate characterization of pore bodies and pore-pore connectivity in order to compute increasingly complex multi-phase drainage (and imbibition) flows. Throat characterization plays an important role in pore-pore connectivity.

The advent of XCMT at energies and luminosities sufficient to produce 3D images of geologic samples has spurred the development of a number of computational throat-finding algorithms[13,20-23], all of which define throats based upon a general definition, “a local minimum

cross-sectional area position." However, we found that these algorithms do not explicitly account for the fact "throats may intersect each other."[24]

We have analyzed XCMT of reactive experiments using the pore network model as well as other image analysis techniques[25]. High temperature, highly alkaline, radioactive waste solutions have leaked from underground nuclear waste storage tanks and associated pipelines into subsurface sediments at the U.S. Department of Energy's Hanford site in Washington. The waste solution strongly dissolves silicates. Released Si reacts with Al, Na and tank waste anions (NO_3^-, CO_3^{2-}, and OH^-) to form secondary precipitates. A body of work has focused on identifying and quantifying the effect of variables (e.g. pH and temperature) governing reaction rates[26-29]. Our interest is to document the amount, character and spatial distribution of these dissolution and precipitation processes and their effects on the pore-network. The principle tools of the Pacific Northwest National Laboratory (PNNL) consist of reactive flow column experiments on Hanford soil models subjected to simulated tank waste leachate (STWL) coupled with XCMT for 3D characterization at time-points during the flow. The imaging methods are combined with computational analysis tools to extract quantitative information.

In initial work[30], large diameter columns were imaged at 40 μm voxel size; however the voxel size allowed only qualitative interpretation of the effects of dissolution and precipitation on changes in the pore-network. In follow-up work[7] utilizing 4 μm voxel size and a flow column of 3.1 mm inner diameter packed with narrow range of grain-sizes (212-300 μm) representative of Hanford coarse sand, it was possible to quantify changes in porosity and in the pore-network structure (changes in distributions of pore volume, throat area, and path tortuosity). As the STWL contained Al ions, these changes were induced by a combination of Si dissolution and secondary precipitation. Estimates of dissolution and precipitation rates as well as porosity

changes based upon effluent concentration measurements of Si and Al in column packs of pure sand grains were presented in Wang and Um[31].

The goal of the discussion is to re-examine throats and to perform 3-D image analysis for reactive experiments. In §2 the image analysis techniques and materials are described. In §3 we discuss a simulated drainage process whose Haines jumps clearly demonstrate the existence of intersecting throats and develop a throat-finding algorithm that allows for the existence of intersecting throats. Next, we discuss the results of the application of our algorithm to XCMT images of Fontainebleau sandstones as well as an unconsolidated soil sample, comparing the performance of this new algorithm against the algorithm described in *Prodanovic et al.*[32]. This latter algorithm, hereafter referred to as PLS, combines the techniques described in *Lindquist and Venkatarangan*[20] and *Shin et al.*[21]. In §4 we analyze the XCMT images of flow columns; in particular concentrate on an estimate of the intra-granular dissolution and precipitation processes as well as document the increasing complexity of the pore network resulting from these processes.

Chapter 2

Material and Methods

2.1. Reactive experiment

2.1.1. Sample S

Quartz sand (200-300 μm size fraction) was wet-packed[7] into the two PolyEtherEtherKetone (PEEK) columns (inner diameter 2.1 mm; length 100 mm) which were named Sample S3 and S4. STWL containing Al flowed through S3 sequentially, whereas S4 was sealed after filled with STWL; there was no additional injection into S4. S3 was sealed between flow experiments. Temperature of S3 was increased from 45°C to 89°C after day 306. The details about the experiments are in Table 1 in *Wang and Um*[31].

2.1.2. Hanford sample

Two intermediate size PEEK columns (inner diameter 19.1 mm; length 91 mm) were also wet-packed[7] with Hanford coarse sediment (1-2 mm size fraction). Hanford Site sediments mainly consist of silicate minerals, including quartz, feldspar, mica (biotite and muscovite), smectite, and basaltic rock fragments[33]. STWL flowed through the columns under saturated conditions at 89°C. The flow rates for both columns were held constant at 0.18 mL/h (0.5 PV/day). The column exposed to the STWL containing Al was subjected to reactive flow over two time periods (Table 1) for a total of 241 days at a temperature of 89 °C. The column exposed

to the STWL without Al was subjected for 261 days at the same temperature. For brevity, these two columns shall be referred to as H_{pre} and H_{dis} respectively.

Table 1. STWL exposure history for each column experiment

Column	H_{pre}		H_{dis}	
Start time	11/11/11	4/12/12	10/28/11	4/12/12
End time	2/15/12	9/10/12	2/15/12	9/10/12
Duration (days)	90	151	110	151

2.2. XCMT imaging

At Brookhaven National Lab (BNL), 3-D XCMT imaging was done six times on four sections (section 1, 2, 3 and 4) of the column S3; 23 days before injection; after 119, 175, 274, 344 and 420 days of the first injection. We refer to these time-points as d_{-23}, d_{119}, d_{175}, d_{274}, d_{344}, and d_{420}. S4 was imaged at five time points (d_{119}, d_{175}, d_{274}, d_{344}, and d_{420}) on four sections. The XCMT image voxel length was 3.96 μm. Each section image, in general, covered 2.4 mm of length of the column (3.96 μm × 600 slices).

At PNNL, 11.3 μm resolution images were taken for H_{pre} and H_{dis}. Column H_{pre} was imaged at three time-points: prior to injection of STWL; after the first 90 days of flow; and after 241 cumulative days of flow. We refer to these time-points as t_0, t_{90} and t_{241}. Column H_{dis} was imaged at time-points t_0, t_{110} and t_{261}. At each time-point, three XCMT images were taken on sections of the column named Sec1, Sec2, and Sec3. Sec1 was located at the inlet and Sec3 was near outlet. Sec2 was between Sec1 and Sec3. In general each imaged section covered 17 mm of length of the column (11.3 μm × 1500 slices).

2.3. 3DMA_Rock

3DMA_Rock is a software package to analyze 3-D images of porous media[34]. It supports segmentation of tomography images, medial axis computation[35], throat finding, pore network construction, and other things.

2.4 Image segmentation

We have used indicator-kriging[36] for segmentation, which performs two-phase segmentation (void and grain). When we input two threshold values T_0 and T_1, indicator-kriging defines the voxels having CT values less than T_0 as void and those having CT values greater than T_1 as grains. The voxels having CT values between T_0 and T_1 are determined by the indicator-kirging method based on their CT values and their neighbors' values.

Multi-phase segmentation using indicator-kriging was done as follows. Let an image contain four phases (gas, liquid and two grains, grain 1, and grain 2). First, we separated the grain space and the non-grain space. Next, after setting the grain space as the region of interest, we separated grain 1 and grain 2. Finally, we separated gas and liquid by assuming the non-grain space as the only region of interest.

2.5 Image registration

In order to compare images over time, image registration (XYZ translation and rotation) of successive images is necessary. Registration was based on segmented images. Registration mainly consisted of two stages, a coarse registration sequence followed by a finer registration. The coarse registration consisted of sequential XY translation, angle θ rotation, and Z translation. Since the sample column is cylindrical (each XCMT slice had a square cross section

which extended beyond the inner walls of the imaged column), all registration computations were performed within a cylindrical region of interest, the radius of the cylinder adjusted to be slightly smaller than the inner diameter of the column. Let $I_2(i,j,k)$ denote an indicator function having a value of: 1 if the voxel (i,j,k) is of phase type grain (or specific phase, e.g. grain 2); and 0 otherwise. Let

$$g(i,j) = \sum_k I_2(i,j,k). \tag{1}$$

The function $g(i,j)$ is a vertical projection through a segmented image stack that counts the number of grain voxels having the same i,j coordinate. Let μ and σ denote the mean and standard deviation of the values $g(i,j)$. Consider the 2D projection of the 3D image,

$$P(i,j) = \begin{cases} 1, & \text{if } g(i,j) > \mu - 3\sigma, \\ 0, & \text{otherwise.} \end{cases} \tag{2}$$

An initial XY translation registration was performed by calculating the projected image center of mass coordinate

$$\left(\frac{1}{n_0}\sum_{P(i,j)=1} i\,, \frac{1}{n_0}\sum_{P(i,j)=1} j\right) \tag{3}$$

where $n_0 = \sum_{P(i,j)} 1$, for each projected image. After calculating all centers of mass of $P(i,j)$ of segmentated images, the images of same section were registered to have coincident projected centers of mass.

Consider the polar rotation $(\tilde{x},\tilde{y}) = R_\theta(x,y)$ (rotation by angle θ about a normal to the projected image through the translated origin). The values in the rotated projection, $P_t(\tilde{x},\tilde{y})$, were obtained by bilinear interpolation from the values $P_t(\lfloor\tilde{x}\rfloor,\lfloor\tilde{y}\rfloor)$, $P_t(\lfloor\tilde{x}\rfloor+1,\lfloor\tilde{y}\rfloor)$, $P_t(\lfloor\tilde{x}\rfloor,\lfloor\tilde{y}\rfloor+1)$ and $P_t(\lfloor\tilde{x}\rfloor+1,\lfloor\tilde{y}\rfloor+1)$ where $\lfloor\cdot\rfloor$ indicates the floor function. Polar angle registration of the three Sec1 images of H_{pre} was performed using the minimization

$$\min_{0\le\theta<360}\sum_{i,j}|[P_t(R_\theta(i,j))-P_0(i,j)]|, \tag{4}$$

where t is a different image time than 0. The polar registration employed angular increments of $\Delta\theta = 0.25°$.

An initial Z registration was then performed using the entire 3D segmented images. Let $I_t(i,j,k)$ denote an indicator function having a value of: 1 if the voxel i,j,k is of grain type (or specific phase); and 0 otherwise. The initial Z registration was performed by the minimization

$$\min_{0\le\Delta\le nz-200}\left(\begin{matrix}\min\limits_{\Delta}\sum\limits_{\substack{i,j,\\0\le k\le nz-\Delta}}|[I_t(i,j,\Delta+k)-I_0(i,j,k)]|\\ \min\limits_{\Delta}\sum\limits_{\substack{i,j,\\0\le k\le nz-\Delta}}|[I_t(i,j,k)-I_0(i,j,\Delta+k)]|\end{matrix}\right), \tag{5}$$

where nz denotes the number of slices in images I_0 and I_t. This ensures that at least 200 slices are registered.

Following coarse registration, a finer XYZ translation registration was performed on the time-sequence of 3D images. For a section for S3, S4, and H_{pre} (samples containing Al), let $I_t^{\mathrm{pre}}(i,j,k)$ denote an indicator function having a value of: 1 if the voxel i,j,k is of grain type; and 0 otherwise. A fine-scale XYZ translation registration was performed by the minimization

$$\min_{I,J,K}\sum_{x,y}\left|\left[I_t^{\mathrm{pre}}(i-I,j-J,k-K)-I_0^{\mathrm{pre}}(i,j,k)\right]\right|, \tag{6}$$

where each of I,J,K ranged in integer value from [−7,7]. The sums in (6) only ran over the overlapped portions of the cylindrical region of interests imposed on I_t^{pre} and I_0^{pre}.

Other section images for H_{pre}, and corresponding images for S3, S4 and H_{dis} were similarly registered with one exception. For H_{dis}, the fine-scale XYZ registration was performed using the minimization

$$\min_{I,J,K}\sum_{x,y}\Delta I_t^{\mathrm{dis}}(i-I,j-J,k-K), \tag{7}$$

where

$$\Delta I_t^{\mathrm{dis}}(i-I,j-J,k-K)=\begin{cases}1, & \text{if } I_t^{\mathrm{pre}}(i-I,j-J,k-K)-I_0^{\mathrm{pre}}(i,j,k)>0,\\ 0, & \text{otherwise.}\end{cases} \quad (8)$$

The minimization in (6) takes into account the possibility that voxels may precipitate or dissolve. The minimization in (7), (8) accounts only for voxels that dissolve and ignores those that appear to precipitate as many of these are assumed to occur during possible grain movement.

2.6 Pore throat network

The pore-throat network enables a statistical comparison (through measures of distributions) of the changes occurring in the pore-network structure as a result of the geometric reactive change. We concentrate only on the flow-accessible part of the pore-network; disconnected pore space was ignored. As disconnected grains are generally unphysical artifacts of segmentation, such grains were converted to fluid phase.

3DMA-Rock uses medial axis paths[35] computed in the void space of a segmented image as a base for throat finding. The medial axis is processed to eliminate from consideration branches of the network upon which no throats exist because either they are "dead end" paths, or they are considered as lying entirely within a single pore body[20]. The dead end paths are removed because there is no way for fluid to flow through them. After this processing, each remaining branch of the medial axis is a likely candidate to contain one or more throats.

3DMA-Rock has used two algorithms for throat finding. One algorithm is to find closed loop (perimeter) of grain surface voxels by dilating a medial axis path[20]. The other is to connect grain surface voxels after finding the closest grain voxel to a medial axis path on each wedge[21]. We have used a technique, referred to as PLS in §1, that combines the two algorithms[37] for speed and robustness. A new throat finding algorithm using planar dilation has been developed (§3).

Pores are identified by throats which separate, and therefore connect, pores. However, the generated throat may cross each other, which results in non-clear determination of pores and pore connectivity. In general we have removed a throat having larger throat area if two throats intersect. We discuss this issue in §3.

Chapter 3

Throat Intersection and Throat Finding Algorithm

3.1. Throats

Under quasi-static flow, which we assume for this chapter, the drainage process (a non-wetting fluid f_n displacing a wetting fluid f_w) can be viewed as a mapping between the capillary pressure (the pressure change across the fluid-fluid surface) and the locations of the advancing fluid-fluid menisci (both terminal- and arc-menisci) within the pore network. At any given capillary pressure, P_C, the terminal menisci are at locations where the local geometry of the pore network supports a stable fluid-fluid meniscus of radius *r* given by the Young–Laplace equation

$$P_C = 2\,\sigma \cos\theta / r \tag{9}$$

where σ is the surface tension between the two fluids and θ is the wetting angle determined by the two fluids and the nature of the grain surface. (For simplicity, we have written the Young-Laplace equation as for cylindrical geometries rather than using the more general form with two principle radii of curvature. This simplification does not affect the point of the discussion – the existence of entry menisci.) Usually an $O(\epsilon)$ increase in capillary pressure results in an $O(\epsilon)$ displacement in a terminal meniscus and an $O(\epsilon)$ volumetric displacement of f_w by f_n. However, when a terminal meniscus reaches a "throat position", an $O(\epsilon)$ increase in capillary pressure eventually results in an $O(1)$ displacement of the terminal meniscus until the meniscus again finds itself in a stable location. (Displacements may be accompanied by the formation of wetting films and an $O(1)$ displacement may be accompanied by splitting of the terminal meniscus or

even merger with another terminal meniscus.) An $O(1)$ displacement is known as a Haines jump[16] and results in a measureable $O(1)$ volumetric displacement of f_w by f_n. We refer to the stable terminal meniscus immediately prior to a Haines jump as an "entry" meniscus; the capillary pressure causing the jump is referred to as the entry pressure P_C^e, which is related to the radius of curvature r_e of the entry meniscus by (1). Since the Haines jump occurs at constant value of P_C^e, the jump must terminate with the terminal meniscus at the first downstream location that supports a stable meniscus having radius of curvature r_e.

The capillary pressure must monotonically increase to continue to drive the displacement process. As is well known from mercury porosimetry measurements[11], micromodel experiments[38], theory[15], and computational simulations[39-41], successive Haines jumps can only occur at positions corresponding to a decreasing sequence of values of r_e. Thus the drainage process is characterized by a sequence of pre-Haines-jump positions in the pore network referred to as "throats" and the *concept of a throat derives its physical significance* from the drainage process. We make the following observation:

D0. The position of an "entry" meniscus under quasi-static drainage provides an experimentally measureable determination of a throat location in a pore network.

Observation D0 does not precisely define the throat; the natural definition derived from D0 is:

D0′. A throat is identically the entry meniscus surface.

In everyday practice in the field of porous media, however, we have come to think of a throat as an intrinsic geometrical property of the pore network structure. We make statements such as "drainage is governed by the smallest throats and imbibition by the largest pores", implying that a pore network structure intrinsically contains throats that "govern" – rather than

"are defined by" – drainage processes. This practice prompts us to critically re-examine the throat concept. In the remainder of the discussion we shall reserve the word "throat" for a drainage-independent, geometric quantity and consider the following two questions. 1) How completely can a throat be defined in a manner *independent* of a particular drainage process? 2) What is the precise characterization of a throat?

Regarding the first question, throats can only be defined independently of drainage if the throat location does not change from one drainage process to the next. This is problematic for two reasons. As shown in Figure 1, the location (and shape) of the entry meniscus changes somewhat with wetting angle. This variation is arguably small and it is reasonable to require that the location of a throat be within the range of entry meniscus positions exhibited under variation of wetting angle. As drainage can occur in either direction down a channel, it is reasonable to require that

T1) a throat approximate an average entry meniscus location, where the average is over wetting angles and possible flow directions.

As mentioned, there is a second problem. In the channel cross sections sketched in Figure 2 (cylindrical symmetry assumed for simplicity) the location indicated by "a" will be the only entry meniscus location for any drainage process through the channel moving from left to right, while the locations indicated by "a" and "b" will be the two entry meniscus locations for any drainage process moving through the channel from right to left. If throats are to be defined independently of a drainage process, then both locations "a" and "b" are throats and we must accept that

T2) not all throats will contribute in every drainage process.

T1 and T2 decouple the definition of a throat from the drainage process. These observations reinforce the following definition:

D1) a throat is a position of local minimum cross-sectional area in the void network, which concurs with the general understanding of a throat[10,11,42-45].

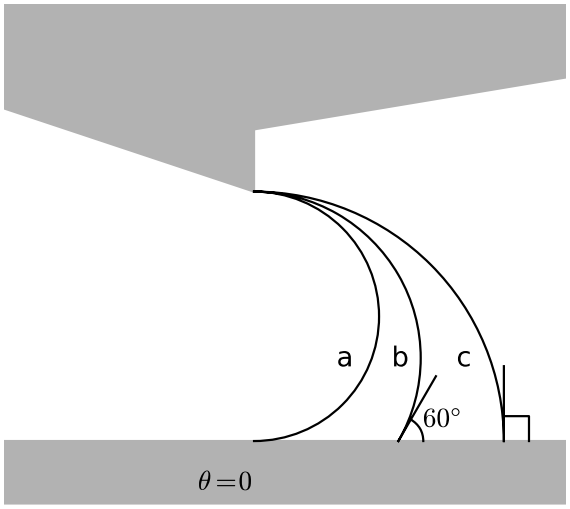

Figure 1. Meniscus position prior to Haines filling of the downstream (right hand) pore during drainage depends on wetting angle, as illustrated here for wetting angles 0°, 60°, and 90°. Void space is white, grain is gray.

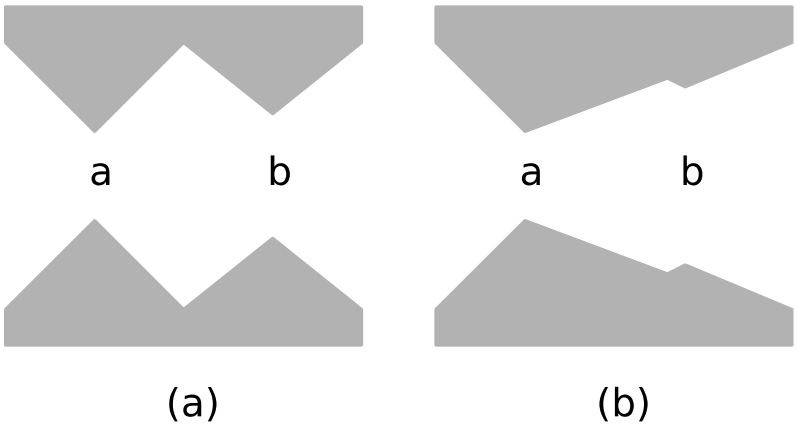

Figure 2. (a) For drainage from left to right, only the constriction "a" acts as a throat. For drainage from right to left, both constrictions "a" and "b" act as throats. (b) Here constriction "b" is less "significant". Void space is white, grain is gray.

As mentioned in §1, there exist computational throat-finding algorithms[13,20-23], all of which define throats based upon definition D1. This generally accepted definition requires some ad-hoc decision making to implement. By straightforward application of D1, each of the locations "a" and "b" in Figure 2b acts as a throat in a drainage process invading from the right. However, it can be argued that location "b" is not a "significant" throat, being merely a minor perturbation in the local throat cross sectional area. (Note however that, in a careful porosimetry experiment, an $O(\epsilon)$ pressure increase above the entry pressure associated with location "b" will result in a sizable right to left meniscus motion.) Given an accurate depiction of the roughly surfaced, irregular geometry in real geologic porous media, it is easy to see that "minor" local minima in the cross section *occur constantly.* There is no convention regarding what is "minor"; in practice, throat-finding algorithms make individual decisions on which "minor" local minima they will ignore. (E.g. the maximal ball method of *Silin and Patzek*[22] uses a well-defined overlapping-ball-centers criterion.) *Glantz and Hilpert*[23] suggest that persistent homology [46] may provide an answer to this question. This is an area to be investigated.

We now address the second question, what quantities should be used to characterize a throat? Is it only a location? – in which case it would be properly described by a perimeter, that is by a topological ring inscribed on the grain surface "circling" the channel at the appropriate location. Mayer-Stowe-Princen (MSP) theory, which analytically specifies the quasi-static flow condition on r_e for piston-like entry of f_n into a channel of constant cross sectional area occupied by f_w, contains both perimeter and area terms related to the invading f_n[15,17,47]. Approximations to this theory, such as *Hwang's*[48] hydraulic radius, strongly suggest that the ratio A/P of the throat area, *A*, and perimeter, *P*, captures most of the variance in predicting r_e for realistic channels[14]. (Alternately expressing Hwang's radius as $r_e = GP$ suggests that the perimeter and the dimensionless shape factor *G* are the two primary throat characterizations. To first order, $G = A/P^2$.) Note that in MSP theory, the area of the (curved) entry meniscus surface does not enter into consideration. However MSP theory deals with channels of constant cross section, which reduces to a planar 2D problem. In extrapolating to 3D, we propose the above observations argue that:

T3) the appropriate characterizations of a throat are the area of the local minimal-area cross section and its perimeter (which defines its location).

Under T3 note that if the throat surface is simply connected, it will have a single perimeter (a topological ring inscribed on the grain surface circling the channel). However if the throat surface is not simply connected, its perimeter consists of a union of n disjoint "rings", $n-1$ of these rings encircling "grain intrusions" piercing the throat surface. A throat finding algorithm must be capable of handling both connectivity possibilities.

Having identified the appropriate throat quantities, one is still left with the problem of computing them. As example, the throat-finding algorithm in *Lindquist and Venkatarangan*[20]

locates a throat by finding a minimum length perimeter (having unit winding number) for each channel (or appropriate subsection of each channel). Given the perimeter, its minimum spanning area is approximated by a triangulation centered on a point assumed to be the center of the throat surface. In *Shin et al.*[21] the cross sectional area is minimized, after which the perimeter of the minimum area is computed. In *Silin and Patzek* [22], the center, circumference and circumference area of a locally minimum-radius maximally inscribed ball defines a throat. Under definition D1, the main difficulty in computing minimal-area cross sections is that they are, in general, non-planar. The computational work needed to accurately compute the required minimal area surface would be prohibitive for software that must compute tens of thousands of throat locations in typical 3D XCMT images of geologic porous media. Consequently the minimum-area cross sectional required in definition D1 must typically be approximated.

In general we have found that existing throat-finding algorithms work acceptably i) for geologic media with porosities 20% or less, and ii) in special cases of high-porosity media if pores are very regular in shape[21]. As discussed in §1, however, for geologic media exceeding 20% porosity, especially unconsolidated material, we find that existing algorithms do not explicitly account for the fact that:

T4) throats may intersect each other.

The existence of intersection throats is demonstrated by using drainage simulation on artificial samples and an algorithm allowing intersecting throats is developed.

3.2. Drainage Simulation

Drainage simulation was performed by using LSMPQS[49] which simulated two-phase immiscible fluid displacement in 3-D using the level set method. We utilized LSMPQS to simulate drainage at a contact angle of 0°. Two artificial samples were used for the simulation.

First sample is very a simple rectangular sample in Figure 3 which has six pores connected through channels. Channels have different size controlled by channel height in Figure 3(b) and they interconnected. In other words, throats intersect each other, since each channel has constant cross-sectional shape and acts as a throat.

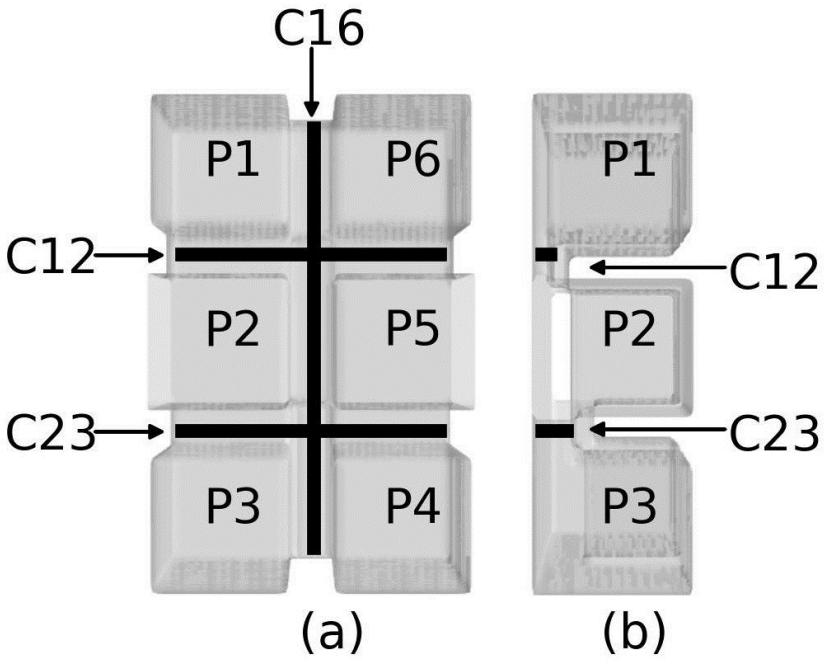

Figure 3. (a) Front and (b) side views of a rectangular 6-pore network joined by vertical and horizontal channels. The pores are labeled P1 through P6. The channel connecting pores *i* and *j* is labeled Cij. The connecting channels C12, C23 and C16 are indicated. Throats are indicated by solid lines. C12 has a smaller throat than C23. Throats in channels C12, C16, C56 and C25 intersect.

Figure 4a-d show the drainage process using LSMPQS with red fluid entering the network from a reservoir connected to pore P2. Fluid exited the network into a reservoir connected to pores P4, P5 and P6 on the right. Initially the capillary barriers due to the throats C12, C25 and C23 retained f_n in P2 (Figure 4a). The first Haines jump occurred into P1 (Figure 4b). Throat sizes were such that the jumps into P5 and P6 occurred within the ΔP_C chosen as the capillary pressure change driving each step of the drainage simulation. Throat C23 was the site of the next Haines jump (Figure 4c), followed by C45 (Figure 4d). In Figure 4d, C34 had yet to be filled with f_n. Figure 4e shows a snapshot of a vertical drainage simulation through the same network. Here the order of throat breakthrough was C16, C12 (Figure 4e), C25/C56, C23 and C45. In particular note in Figure 4a, c and e how throats, intersected at right angles to each other, correspond to locations where the drainage interface is held in check.

Accepting T4 leads to the understanding that complex geometric scenarios can occur, three of which are sketched in Figure 5, showing two (Figure 5a), three (Figure 5b) and four (Figure 5c) intersecting throats. Examination of Figure 5c opens another question. Does this 2D sketch represent four throat surfaces (as labeled) that meet along a common line (in 3D), or are these two throat surfaces that pass through each other. Based upon the example of Figure 3 we propose a fifth throat condition:

T5) a single throat must uniquely separate two distinct pores.

Condition T5 argues for the throat labeling shown in Figure 5.

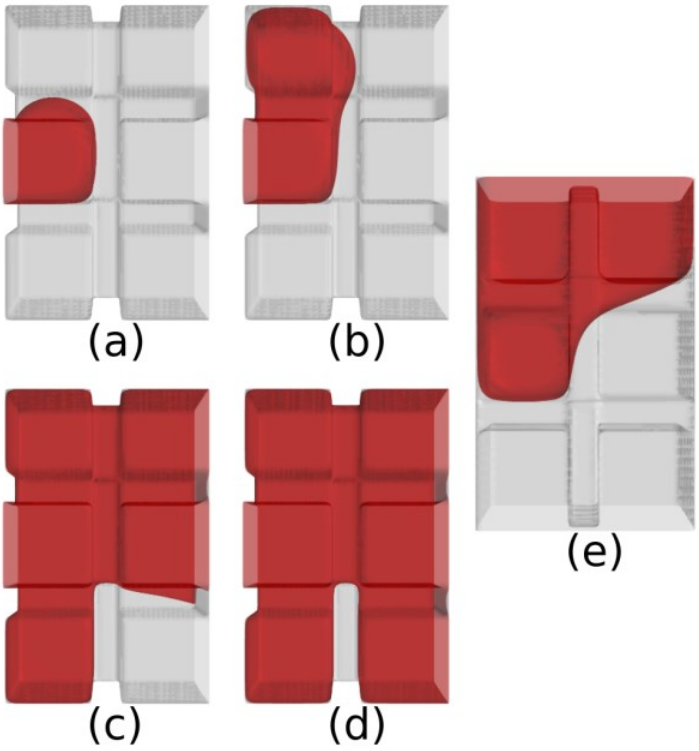

Figure 4. Snapshots of an LSMPQS drainage simulation through the pore network of Figure 3. (a-d) Pore P2 was connected to an inlet reservoir holding f_n (red fluid); pores P4, P5 and P6 were connected to an outlet reservoir. (e) A single snapshot of a simulation in which pores P1 and P6 were connected to the inlet reservoir and pores P3 and P4 were connected to the outlet reservoir.

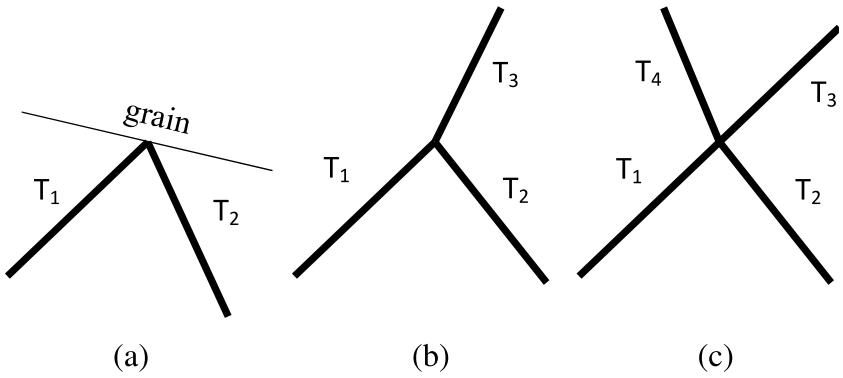

Figure 5. Possible cases for throat intersection including (a) two, (b) three and (c) four intersection.

3.3. An algorithm for Intersecting Throats

To our knowledge, none of the existing throat finding algorithms makes any systematic effort to account for the possibility of intersecting throats. To address this, we have developed a new throat finding algorithm for the 3DMA-Rock package which explicitly allows for this necessity.

Our new algorithm, called the planar dilation (PD) algorithm, makes a concession for speed and robustness by approximating throats by planar surfaces. As discussed in the Introduction, throat surfaces are generally expected to have curvature. Consequently, we compared the results of the new algorithm against computations performed by the existing PLS algorithm which does allow for curved throats. The heart of the new algorithm is the ability to rapidly construct a "plane" of 6-connected voxels at an arbitrary θ, φ (spherical angle coordinates) orientation passing through a specific medial axis point. We refer to this set of voxels as a throat barrier. (3DMA-Rock treats the void space in digitized image as 26-connected. To separate pores, the throat barrier must be a 6-connected assemblage of voxels.) The barrier contains within it the analytic, 2D planar throat surface whose perimeter and area will be used to characterize the throat.

Two general considerations were built into the algorithm design. 1) Since, in drainage, smaller throats control the flow prior to larger ones the algorithm preferentially finds smaller area throats first. 2) However, if the algorithm needs to choose between two throats of similar area (we employ a < 5% area difference as a criterion for similar) in a channel, a non-intersecting throat is chosen in preference to one that intersects others.

The core of the planar dilation algorithm comprises the construction, starting from any given "base" voxel on the medial axis, of a plane cross section surface – a throat – and a 6-

connected "barrier" of voxels, each such voxel intersecting the throat surface. Let *v* denote the current "base" voxel. The center of *v* is referred to as the base point. A least-squares fit using the base point and the center points of the 6 neighboring medial axis voxels to *v* is used to establish the local tangential direction, $\hat{t}$, to the medial axis. The tangential direction acts as the zenith-axis in a spherical coordinate system centered at the base point. A polar angle θ relative to the zenith-axis, and an azimuthal angle φ in the plane perpendicular to the zenith-axis (for fixed θ, φ is measured relative to the x-axis of the digitized medium) determine a normal vector, $\hat{n}_{\theta,\varphi}$. This normal vector is the normal to the plane $P_{v,t,\theta,\varphi}$ around which the throat barrier is constructed (Figure 6).

Computation of the throat barrier proceeds as follows. Starting at *v,* we run a 26-connected dilation process through successive neighboring void voxels retaining only those that intersect the plane $P_{v,t,\theta,\varphi}$. Those so retained are the desired barrier voxels. The precise test for whether the plane passes through a void voxel *w* involves the computation of 8 inner products, $w_i,\ i = 1, \ldots, 8$, where w_i is the inner product between the normal vector $\hat{n}_{\theta,\varphi}$ and the vector from the base point to corner *i* of voxel *w*. If $w_i > 0$ then corner *i* lies above the plane; if $w_i < 0$, corner *i* lies below the plane; if $w_i = 0$, corner *i* lies on the plane. If $w_i > 0,\ i = 1, \ldots, 8$ or $w_i < 0,\ i = 1, \ldots, 8$ then $P_{v,t,\theta,\varphi}$ does not pass through *w*, and *w* is not a barrier voxel. If $w_i > 0$ and $w_j < 0$ for $j \neq i$, then $P_{v,t,\theta,\varphi}$ passes through *w*, and *w* is taken to be a barrier voxel. Two cases remain: a) $w_i \geq 0,\ i = 1, \ldots, 8$ or b) $w_i \leq 0,\ i = 1, \ldots, 8$ with $w_j = 0$ for at least one corner *j*. In case a) we decide that *w* is a barrier voxel; in case b) we decide *w* is not a barrier voxel. This choice guarantees that the barrier remains minimally 6-connected. (Allowing both case a) and b) to define a barrier voxel would produce barrier voxels whose removal would leave the barrier still 6-connected. Rejecting both case a) and b) as barrier voxels would generate

barriers that were not 6-connected.) The dilation process, beginning from voxel v, terminates when all successively neighboring void voxels have been eliminated as possible barrier candidates.

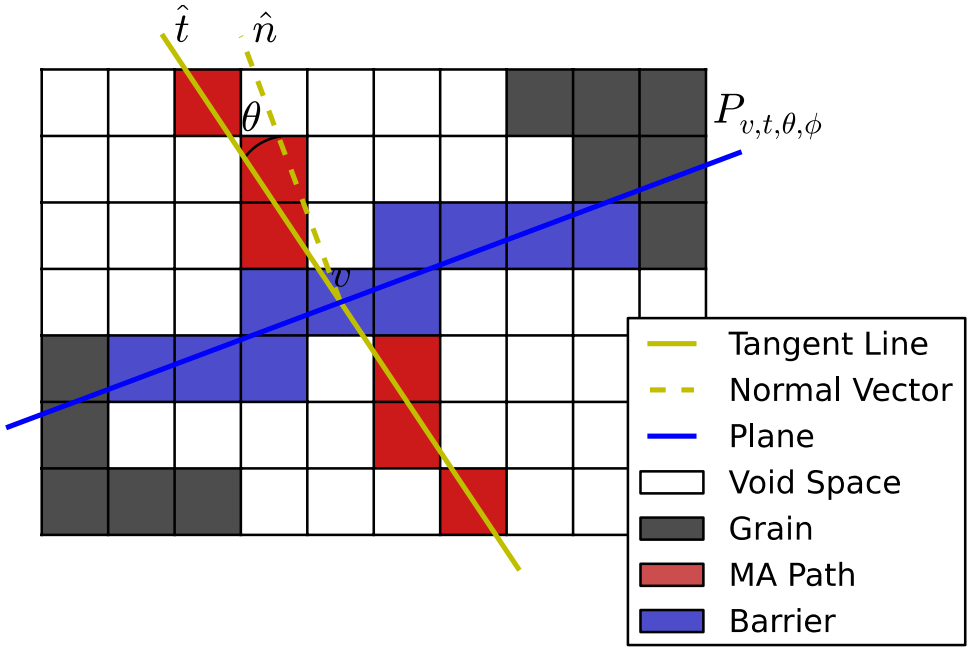

Figure 6. 2D ($\varphi = 0$) illustration of the procedure used to find throat barriers. Voxel v is the current medial axis voxel at which the computation is performed. $\hat{t}$ is the local tangent line to the medial axis at v; the vector $\hat{n}$, oriented at spherical angles $\theta, \varphi = 0$ to $\hat{t}$, is the normal to the plane $P_{v,t,\theta,\varphi}$. The throat barrier voxels, all of whom are intersected by $P_{v,t,\theta,\varphi}$ must be 6-connected to separate the channel into two 26-connected void phases (pores).

It is straightforward geometry to compute the area of the section of $P_{v,t,\theta,\varphi}$ that intersects each barrier voxel. The cross-section area of the throat is defined to be the sum of these sectional areas. It is similarly straightforward to compute the perimeter of the constructed throat. Consider the face between a barrier and a grain voxel that are 6-connected. The intersection of this face and the plane $P_{v,t,\theta,\varphi}$is a line segment. The union of all such line segments for a single throat

barrier forms a "face polygon" that is a candidate for the perimeter of the throat. However, this polygon will have a decided "staircase" shape as it follows voxel faces (solid lines in Figure 7a). We therefore construct a second polygon by linearly connecting the midpoints of sequential line segments of the first polygon (dashed lines in Figure 7). This second polygon is defined as the throat perimeter, and the throat area is recalculated based on this perimeter.

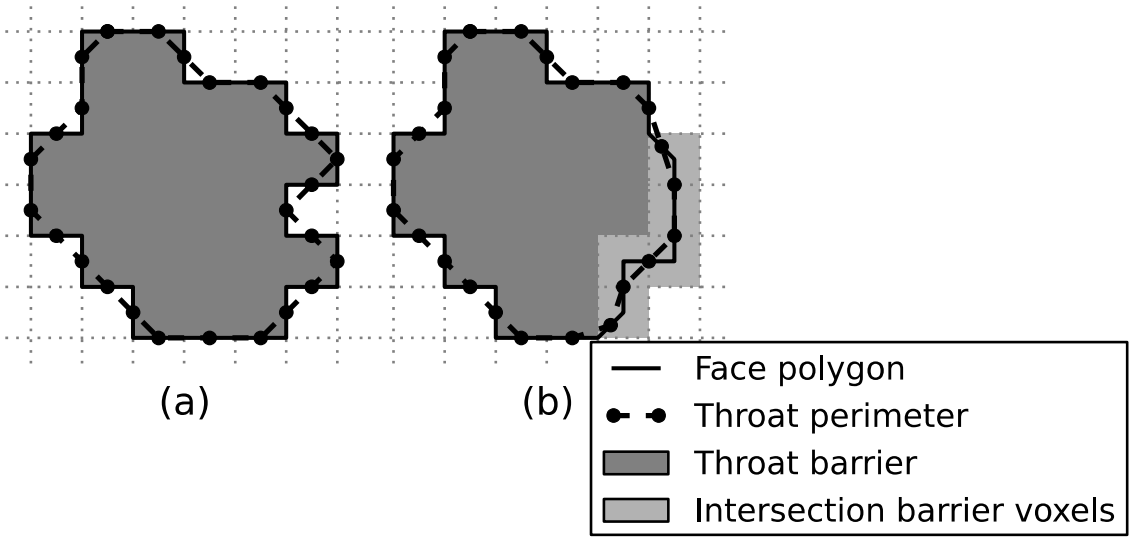

Figure 7. Illustration of perimeter construction for (a) a throat barrier that contacts grain voxels around its entire perimeter; (b) a throat barrier intersecting another throat barrier along part of its perimeter. The view is along the normal direction of the throat plane.

Having explained how to compute a single (candidate) throat surface and corresponding (candidate) throat barrier for an arbitrary medial axis voxel, v, we describe how we compute a minimal area throat, and corresponding barrier, for a medial axis path, p. Again consider voxel v on the path. Recall that the local tangent direction $\hat{t}$ at v acts as the zenith-axis of a spherical coordinate system. Consider the sequence of normal vectors $\hat{n}_{ij}$ defined by the polar and azimuth

angles $\theta_i, \varphi_j,\ i = 1, \ldots, m; j = 1, \ldots, n$. Each $\hat{n}_{ij}$ defines a plane $P_{v,t,\theta_i,\varphi_j}$ upon which to build a throat and its barrier through *v*. By varying normal vectors, we define a discrete optimization stencil over which we can search for a minimal area throat/barrier candidate at *v*. (We used $m = 9, n = 8$ in our computations, with $5° \leq \theta_i \leq 45°$ in increments of 5° and $0° \leq \varphi_j \leq 315°$ in increments of 45°. Together with the choice $\theta = \varphi = 0$, this amounted to the construction of 73 throats/barriers at each voxel *v* on each medial axis path. This required that the computation for each individual barrier be fast.) For voxel *v*, let $A_v = \min_{k=1,\ldots,73} A_k$ where A_k is the throat area computed for the *k*'th throat/barrier in the optimization stencil. Let θ_v, φ_v denote the normal direction corresponding to the throat having area A_v. For each voxel *v* on a path, the information $v, \theta_v, \varphi_v, A_v, B_v$ is stored in a "cross-section" list. (Here B_v represents the information on the barrier voxels computed for this throat surface.) Thus if the medial axis path *p* is comprised of n_p voxels, its cross-section list has length n_p.

We enforce two conditions during throat finding.

Condition 1: For the throat surface computed for any plane $P_{v,t,\theta_i,\varphi_j}$, we compute an effective throat radius $r(A) = \sqrt{A/\pi}$, where *A* is the area of the throat surface. If $r(A) > \min(l_{sv}, l_{ve})$, where l_{sv} is the distance from the base voxel to the start of the medial axis path and l_{ve} is the corresponding distance to the end of the medial axis path, then we ignore this as a throat possibility (i.e. no throat surface is computed for plane $P_{v,t,\theta_i,\varphi_j}$). Condition 1 is *always* applied during the planar dilation process described above. Condition 1 has two primary purposes. It neglects "minor" constrictions of the sort noted in Figure 2b and it also prevents throat construction for a medial axis path that lies entirely within a single pore. As a result of enforcing condition 1, throat construction may "fail" on one or more (including all!) voxels of a path.

Condition 2: This condition deals with throats that, constructed for one medial axis path, intersect a second medial axis path. Condition 2 is only applied to "declared" path throats (whose identification is described in the following paragraphs). Consider medial axis path i having throat t_i of area A_i and effective radius $r(A_i)$. Assume t_i intersects medial axis path j ($j \neq i$) at voxel v_j. When the planar dilation algorithm runs on path *j,* those voxels of path j lying within a distance $r(A_i)$ of v_j are excluded from consideration. $r(A_i)$ is therefore an effective exclusion volume. If path *j* is intersected by declared throats from several other paths, it is possible that the entire path *j* lies in excluded volumes, and no throat can be computed for path *j*.

As a result of conditions 1 and 2, the cross-section list for path *p* may have fewer than n_p entries (in fact it may be empty). Once a cross-section list has been completed for a path, it is sorted, smallest to largest, by magnitude of A_v. For the path, the surface with the smallest area is considered the current throat candidate and its area and barrier are referred to as the current throat area and barrier. However the remaining computed throats in the cross-section list are retained as possible contenders for the path throat.

The throat finding algorithm consists of three steps followed by sequential iteration of a modified first and third step.

Step 1. The cross-section list is computed independently for each medial axis path. Independence means that the possible existence of throats on other paths does not affect the computation of the cross-section list for any single path *p*. (Consequently, condition 2 is not applied.) At the completion of step 1, paths fall into two groups, G1a) those that have a current area, and G1b) those that do not (cross-section list empty due to application of condition 1). The paths in G1a are ordered according to the value, smallest to largest, of their current areas.

Step 2. A subset of paths whose throats do not intersect each other are declared as follows. The current throat, area and barrier of the first path in G1a (the sorted path with the smallest current area) are declared to be the throat, area and barrier for path 1. The algorithm loops over the remainder of the sorted path list in G1a. For each subsequent path, *i*, throat barriers corresponding to the lowest 5'th percentile in area are examined. The smallest area barrier intersecting none of the previously declared throat barriers, together with its throat and throat area, are declared to characterize the throat for path *i*. Otherwise no throat is declared for path *i* at this point. Condition 2 is applied during this step; if the declared throat barrier for path k passes through a medial axis path $k + j$, then its exclusion volume is applied to the cross-section list for path $k + j$, which is modified accordingly. At the end of step 2, paths now fall into three groups: G2a) those that have a declared (non-intersecting) throat, G2b) those that have current area (throat as yet undeclared), and G2c) those that have no cross-section list. G2b comprises those paths in G1a whose throat barriers intersect with those of other paths. G2c comprises those paths in G1b plus paths whose cross-section lists were eliminated in step 2 as a result of application of condition 2.

Step 3. In step 3, the algorithm declares throats which are terminated by other throats. It examines only the paths in group G2b, addressing them in the same order as in step 2. Let path *j* be one such path. The planar dilation algorithm is rerun for the voxels comprising the lowest 5'th percentile of entries in the cross-section list for path *j*. However, now the planar dilation is blocked whenever barrier voxels from previously declared throats (those in group G2a plus those throats that are declared as the paths in group G2b are processed) are encountered. Condition 2 is applied using all declared throats in step 3. From the throats reconstructed out of this 5'th percentile sample, that with the smallest area (together with its barrier) is declared to comprise

the throat for path *j*. At the end of step 3, paths now fall into three groups: G3a) those that have a declared (non-intersecting) throat, G3b) those that have a declared intersecting throat and G3c) those that have no cross-section list. G3c comprises those paths in G2c plus paths whose cross-section lists were eliminated in step 3 as a result of application of conditions 1 and 2.

Step 1′. The planar dilation algorithm is rerun on all paths in group G3c. For purposes of this dilation, all paths in this group are treated as independent of each other; however their dilated throat candidates are terminated by declared throats in groups G3a and G3b. Condition 2 for all declared throats is applied during the planar dilation of paths in G3c. At the end of step 1′, paths in group G3c fall in two subgroups, G1′a) those with cross-section lists with current areas, and G1′b) those having no current area (the result of application of conditions 1 and 2). The paths in G1′a are sorted according to current area.

Step 3′. Step 3 is rerun on the sorted paths in G1′a.

Steps 1′ and 3′ are iterated until group G1′a is empty.

Steps 1 through 3′ locate, where possible, the smallest area (primary) throat on each path. We allow for the possibility that a path might have more than one throat as in Figure 2a. Multiple throats are located on any path only after primary throats have been found on all paths. Let *p* be a path for which the primary throat is $v_1, \theta_{v_1}, \varphi_{v_1}, A_{v_1}, B_{v_1}$. Consider the remainder of the cross-section list for *p.* Apply the exclusion volume around the throat voxel v_1, as well as enforce any exclusion volumes from other throats (condition 2) that may intersect *p.* The barriers and cross-section areas for the (non-excluded) remainder of the cross-section list must also be recomputed as throats that have been declared in earlier steps may cut through these cross-sections. Moving along *p* on one side of v_1, locate the first (two-sided limit) minimum cross section area located outside of any exclusion region. This is then declared to be the next throat $v_2, \theta_{v_2}, \varphi_{v_2}, A_{v_2}, B_{v_2}$

on p. Establish the exclusion volume around v_2. This procedure is iterated along p, in both directions from v_1, until all local minima (two-sided limit) in non-excluded regions have been located.

Once all possible throats have been declared, a pore-throat network is constructed whereby the entire void volume is distributed into individual pores separated by planar throat surfaces having no volume. During the network construction, post-processing modification of intersecting throats occurs. In line with the discussion of Figure 5, each throat surface must separate exactly two pores. Therefore if one throat serves as a boundary for another, the blocking throat is split appropriately.

This procedure is illustrated in Figure 8. As indicated in Figure 8a, a barrier voxel such as $v_{2,3}$ may border more than two pores. Such barrier voxels are flagged as throat intersection voxels. A throat barrier is split along its set of such intersection voxels (Figure 8b). As a voxel is the unit of digitization, we do not subdivide an intersection voxel. Rather, we assign an intersection voxel to each of the barriers of the intersecting throats (i.e. $v_{2,3}$ is assigned to each of barriers 1, 2, and 3 in Figure 8b), but assign an appropriate partial area to each of the throats intersecting in the barrier voxel. Figure 9 illustrates this procedure with an example. Initially (Figure 9a), throat T_1 blocks T_2. Throat T_1 is split into T_1 and T_3 (Figure 9b); T_1 and T_3 each are assigned one-half of area A_1. Throat T_2 is assigned half of area A_2. (These area assignments are reasonable approximations that avoid a detailed geometrically accurate computation.)

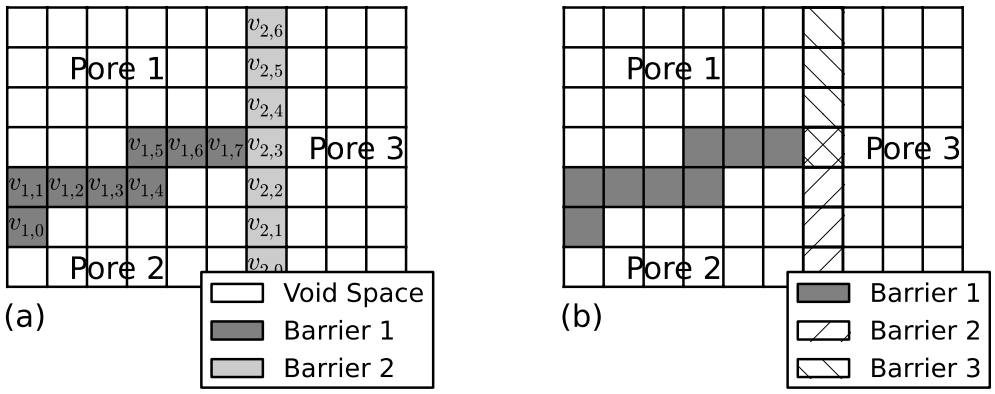

Figure 8. Illustration of the postprocessing step that splits throat barriers. In (a), barrier 2 was constructed first, blocking barrier 1. In (b), the configuration has been split into three barriers.

The existence of throat barrier intersection voxels, which now form part of the boundary of more than one throat, must be taken into account when computing face polygons and throat perimeters. Consistent with the above approximation used for throat area assignments in intersection voxels, face polygons are assigned to run through the centers of barrier intersection voxels as illustrated in Figure 7b (solid line). To reduce staircasing affects, we then modify the face polygons by connecting midpoints − producing the throat perimeter (dashed line).

We have observed that, in the resulting pore-throat network, a pore may have a throat with an area that is large relative to the total surface area of one of the two pores it separates. Based on models of hemispherical pores, we remove a throat if its area exceeds 1/3 of the surface area of either of the two pores it separates. This, of course, results in the merger of the two pores.

Another characteristic related to throats is channel lengths. Previous algorithms in 3DMA_Rock use medial axis path lengths as channel lengths. However, because of splitting, pores or throats in pore-throat networks from PD may not contain any medial axis voxels. Therefore, PD calculates channel lengths by calculating local medial axis from a pore center to a throat center[9].

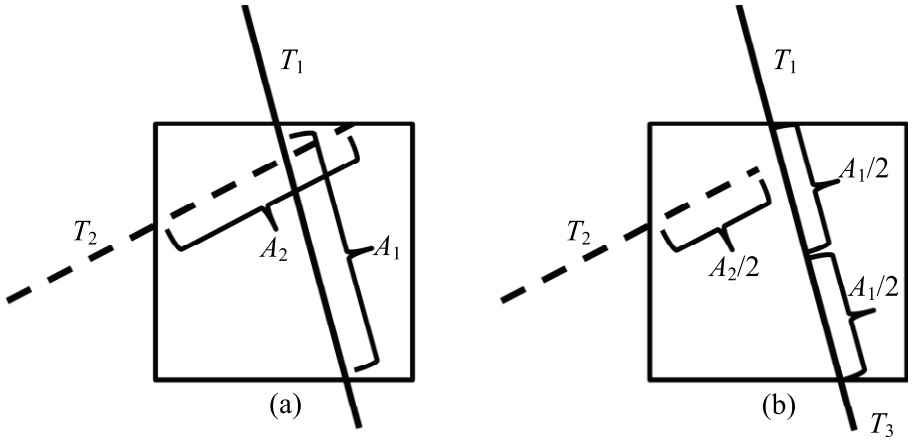

Figure 9. 2D illustration of throat splitting and the assignment of approximate throat areas in an intersection barrier voxel. (a) A_1 and A_2 are the areas of intersection of the barrier voxel with the two throats T_1 and T_2. (b) T_1 is split into throats T_1 and T_3; half of area A_1 is assigned to each of these throats. Half of area A_2 is assigned to throat T_2

3.4. Performance of PD

We run LSMPQS drainage simulation and PD on an artificial example (Figure 10). We claim that the pores labeled 1 and 2 are separated by a throat, so are pores 2 and 3, 3 and 4, and 4 and 1, and that these throats border one another (intersect). The computed throats – there are 32 of them – are shown in Figure 11a. Also, Figure 11 shows snapshots of an LSMPQS drainage simulation (flow from top to bottom). The drainage simulation clearly demonstrates how intersecting throats "act" as independent throats (capillary barriers).

In *Lindquist et al.*[50] pore volume and throat area distributions were computed using the algorithm PLS (which allows for curved throat surfaces) for a suite of four XCMT images of Fontainebleau sandstone samples. The analyzed samples were $550 \times 550 \times 511$ voxels, with voxel size 5.7 μm. Sample porosities were 7.5%, 13%, 18% and 22%, We recomputed the pore-throat network using the new planar-dilation (PD) algorithm. Each algorithm comprises two major phases, identification of all throats followed by construction of a pore-throat network.

Some modification of the identified throats occurs during the network construction phase. For the PD this consists of splitting of “blocking” throats and elimination of large area throats. For the PLS algorithm, this consists of deleting any throat that separates more than two pores. We therefore compare the results of the PLS and PD throat finding algorithms at the end of each of these two phases.

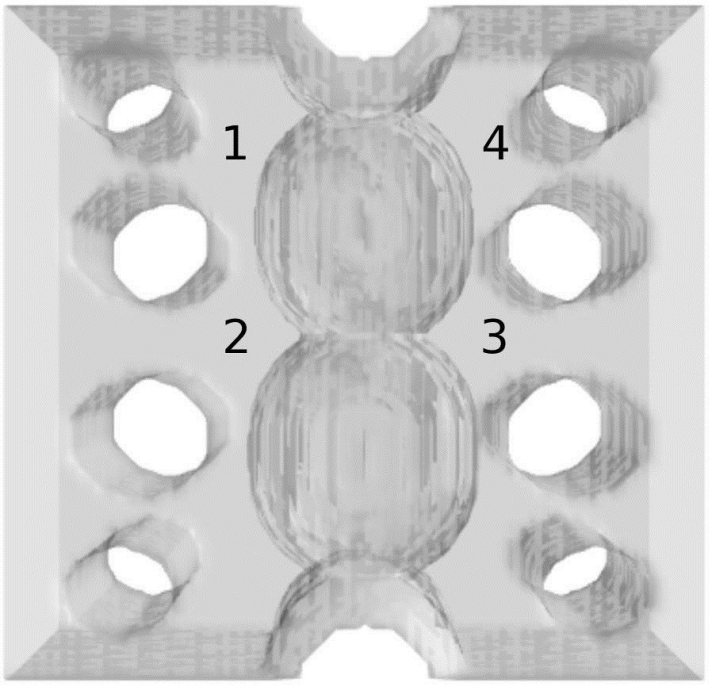

Figure 10. An artificial porous medium consisting of a back and front plate joined by eight solid cylinders, four on the left, four on the right. For representation purposes, the insides of the solid cylinders are not shown—only the cylinder surface. A “column” of two solid spheres “welded” to each other are also ‘‘welded’’ to half-sphere indentations on the bottom and top plates. These two spheres do not contact the front and back plates. There is void space between the plates, cylinders, and spheres. The sample can be sealed on either pair of opposing sides to examine flow through the medium. The numbered regions indicate the positions of four of the interior pores.

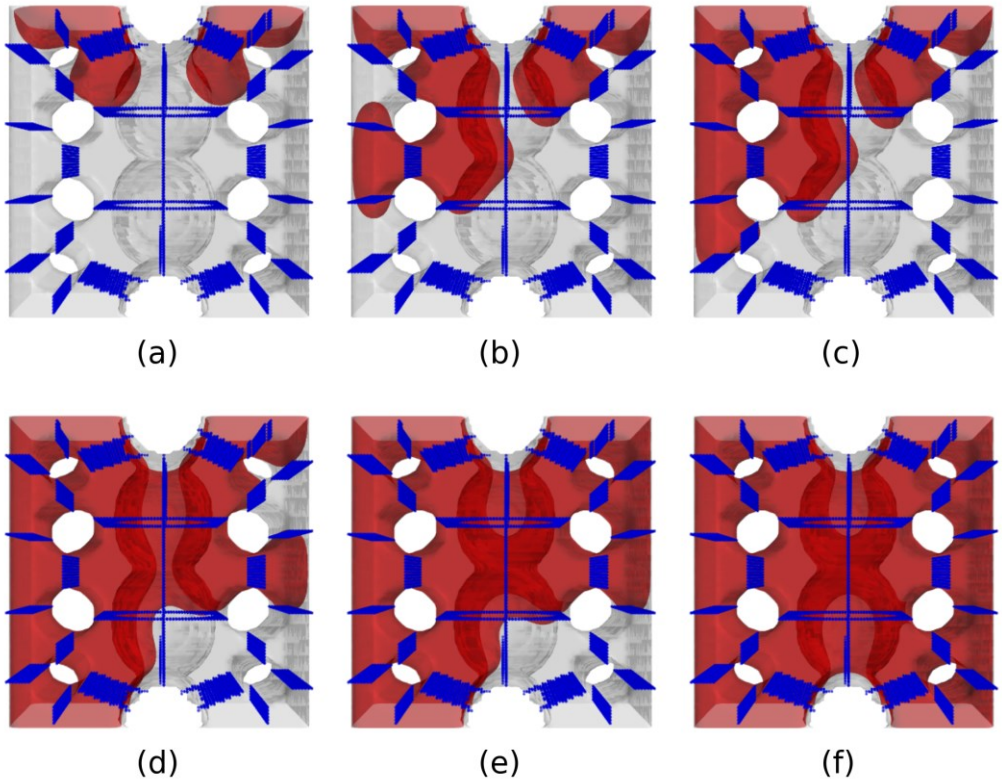

Figure 11. LSMPQS simulation of drainage flow (top to bottom) through the network of Figure 10. The non-wetting fluid is red, wetting fluid is grey. The computed planar throat surfaces are blue. There are 32 throats, 9 on the left side, 9 on the right and 14 running through the middle.

Figure 12 summarizes the throat number density (number of throats per mm^3 of sample) identified in the four Fontainebleau samples by the two algorithms at the end of each of the two phases. The throat density increases with the porosity of the sandstone. After the throat identification phase the PLS algorithm locates 3% to 5% more throats than the PD algorithm. However in its pore-network construction phase the PLS algorithm rejects roughly 10% of the throats, whereas the pore-throat network construction phase of the PD algorithm sees a net gain of throats through throat splitting. Consequently, after the network construction phase, the PD algorithm has a throat number density that exceeds that of the PLS algorithm by 13% to 22%.

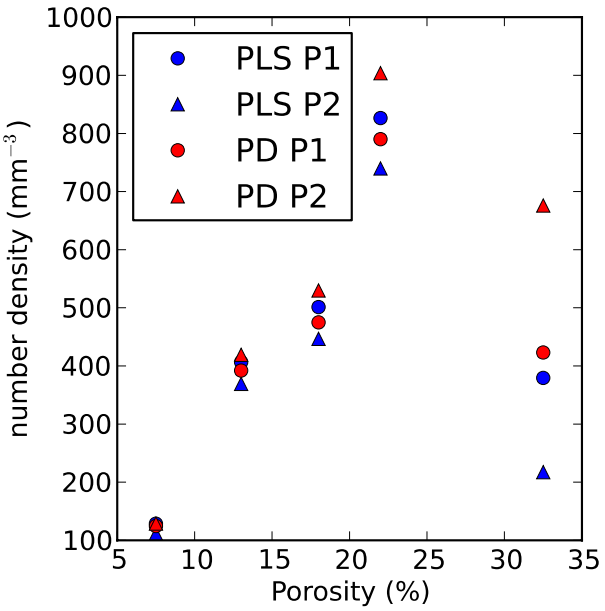

Figure 12. Throat number density as a function of sample porosity as determined by the PLS and PD algorithms after the throat identification phase (P1) and after pore-throat network construction phase (P2).

Figure 13 compares the throat area distributions for the lowest (7.5%) and highest (22%) porosity Fontainebleau samples after the throat identification phase (left plots) and after the network construction phase (center plots). While the overall shape of the distributions is similar, the PLS distribution is shifted slightly to larger area. At the end of the network construction phase, there is a slight difference in the distribution of smaller throat sizes due to the splitting of blocking (intersecting) throats in the PD algorithm. Such throats are discarded in the network construction phase of the PLS algorithm.

The pore volume distributions, available after the pore-network construction phase, are compared in the right plots of Figure 13. The distributions are very similar between the two algorithms.

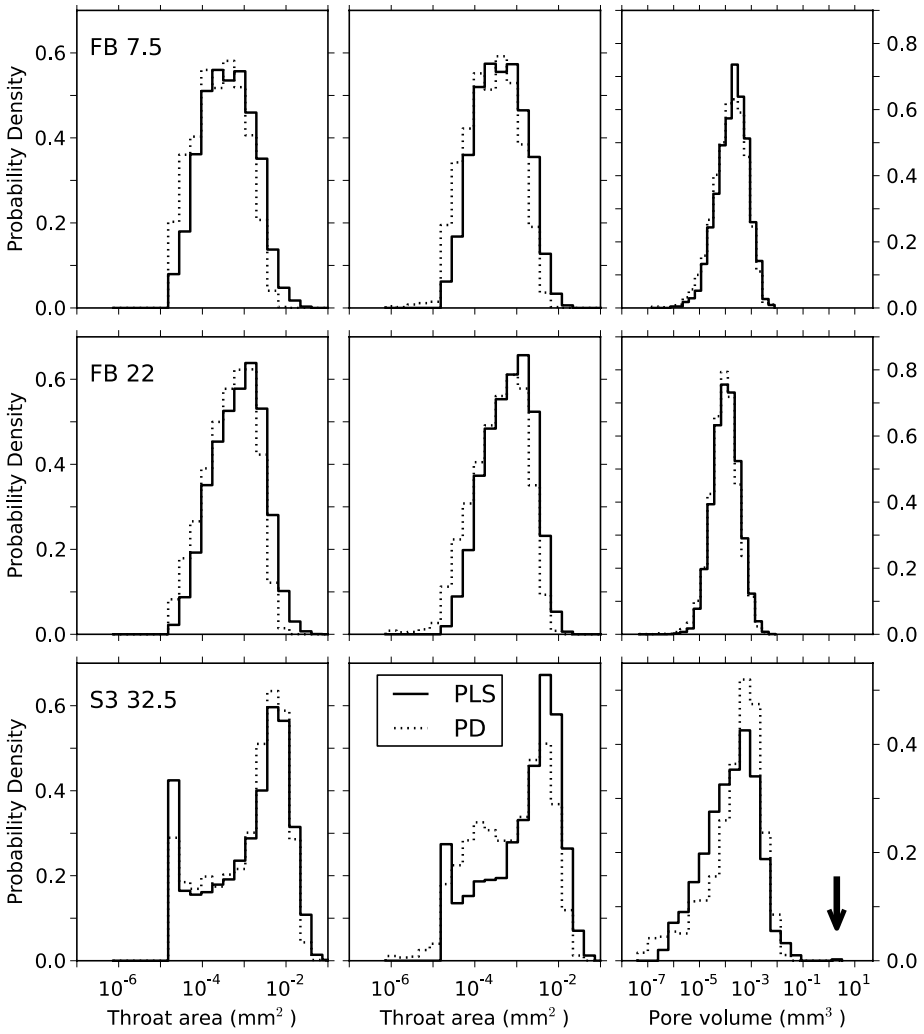

Figure 13. Throat area and pore volume distributions for the 7.5% and 22% porosity Fontainebleau sandstone images (first and second rows) and a 32.5% porosity sample S3 image(third row) using the new PD algorithm compared to the results of the PLS algorithm. The graphs on the left present the distribution of throat area identified during the throat identification phase of each algorithm; the graphs in the center present the distribution of throat areas after the pore-throat network construction phase.

The performance of the PLS and PD algorithms was also compared on sample S3 whose porosity was 32.5%. The analyzed image size was 600×600×700 voxels. Also shown, respectively, in Figure 12 and Figure 13 are the throat number density, throat area and pore volume distribution comparisons obtained for sample S3. In spite of the increased porosity, the

throat number density of this unconsolidated sample is comparable to Fontainebleau samples of smaller porosity. After the throat identification phase, the throat number density is 11% smaller for the PLS algorithm. After the pore-network construction phase, the handling of intersecting throats (retained and subdivided in the PD algorithm, rejected in the PLS algorithm) results in marked differences in the throat number densities. The throat area distributions after throat identification are similar for the two algorithms; after the pore-throat network phase, there are marked differences between the throat area distributions. Rejection of the possibility of intersecting throats by the PLS algorithm has drastic consequences in pore partitioning in S3. The pore volume distributions for S3 show more distinct differences than the lower porosity Fontainebleau comparisons. The pore-network construction for S3 from the PLS algorithm resulted in a largest pore having volume 2.03 mm^3. In contrast, the largest pore constructed by the PD algorithm had a volume of 0.03 mm^3.

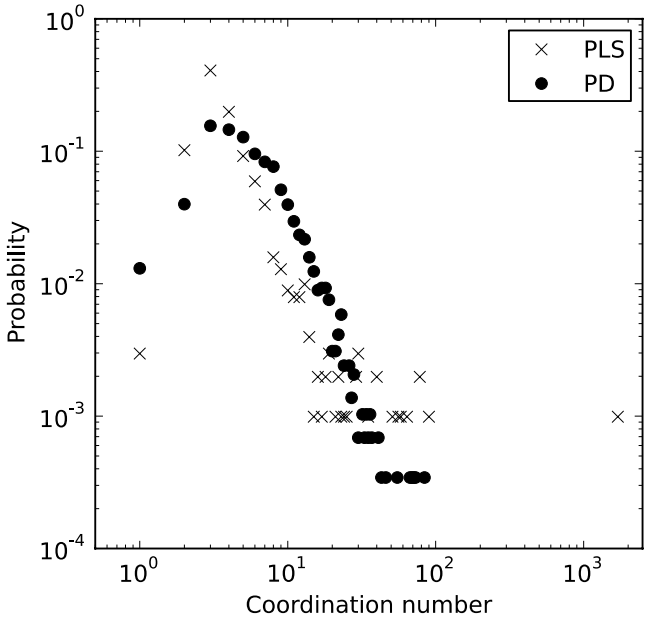

Figure 14. Comparison of pore coordination number distribution computed from the XCMT image of sample S3 using algorithms PD and PLS.

The production of large pores by the PLS algorithm in high porosity samples is the most significant consequence of neglecting intersecting throats. As shown in Figure 14, such pores have very large coordination number. The PLS algorithm also produces significantly more pores having coordination number 2 through 5. The increase of the number of coordination number 1 pores in the PD algorithm is the result of a subtle effect. Throat areas are computed from the planar throat surfaces which cut through barrier voxels; individual pores are identified using the throat barriers – which are digitized at the voxel level. Thus the plane surface passing through a barrier voxel may not come into contact with the grain surface while the barrier voxel itself may contact the grain surface. Since barrier voxels determine distinct pores, this subtle effect may cause a pore to be split into two pieces, with the "split-off" piece commonly being a small, coordination-number 1 pore.

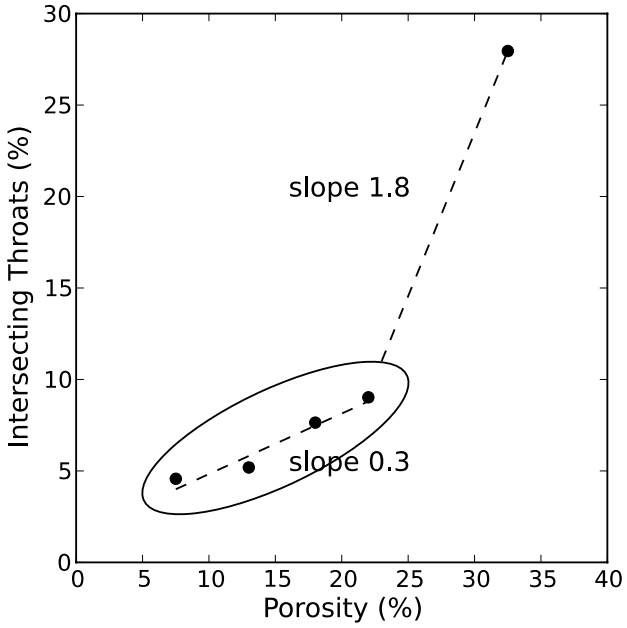

Figure 15. Observed increase in the frequency of intersecting throats (expressed as a percentage of all throats) with porosity.

Figure 15 plots the percentage of all throats that intersect as a function of porosity of the investigated sample. Over the porosity range 7.5% to 22%, the percentage of intersecting throats increased at the rate of 0.3% per percent porosity change. Over the porosity range 22% to 32.5% intersecting throats increased at the significantly greater rate of 1.8% per percent porosity change, indicating the need for throat finding algorithms that capture intersecting throats. For sample S3, 27.95% of all throats intersected with another.

Chapter 4

Reactive Experiment Image Analysis

4.1. Sample S

Figure 16 is a slice image of sample S3. The image size is 2.38 mm × 2.38 mm which is larger than column diameter (2.1 mm). Since the column boundary is invisible in the XCMT images, we set the region of interest based on the grains. There were gas bubbles near boundary, but we ignored them (considered as liquid) because gas easily moved and had little effects on reaction.

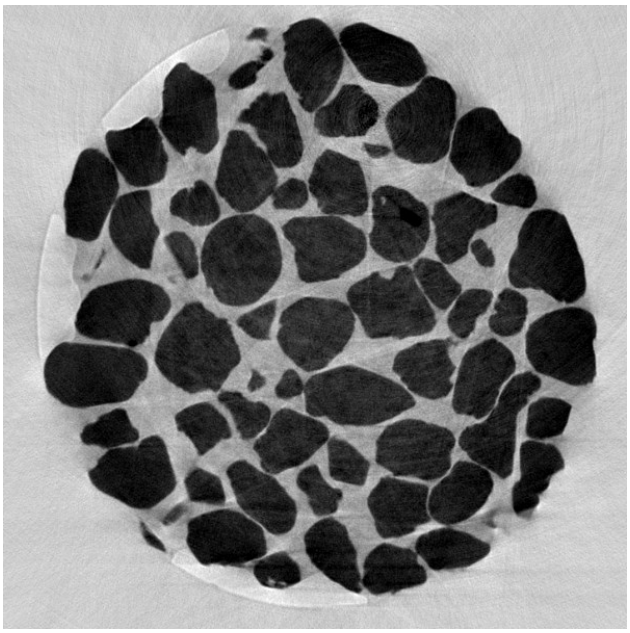

Figure 16. An XCMT slice image of sample S3 section 3 at d_{-23}. Dark color represents high intensity voxels (grain).

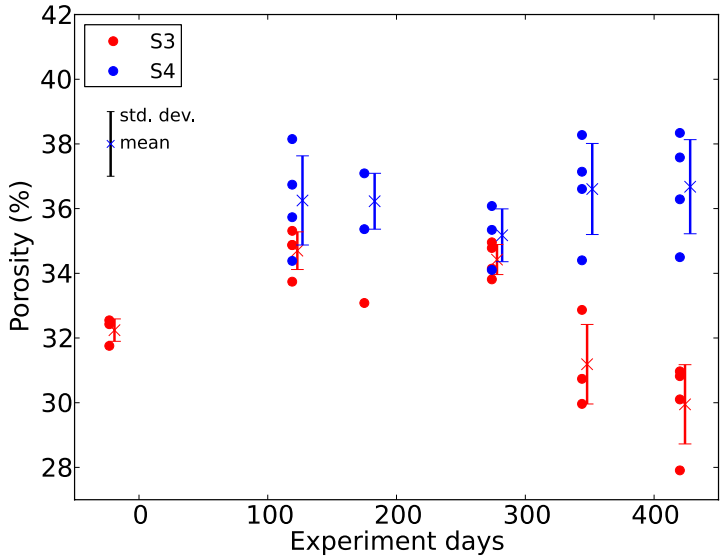

Figure 17. Porosity changes of sample S3 and S4.

The registered (by the method described in §2) sample lengths of sample S3 were 1.43 mm, 1.25 mm, 1.43 mm, and 1.90 mm for section 1, 2, 3, and 4 respectively. Those of sample S4 were 1.84 mm, 2.06 mm, 2.07 mm, and 1.90 mm.

Since STWL contained Al, we expected both dissolution and precipitation. As illustrated in Figure 17, the porosity of S3 first increased (2%) and then, after d_{306}, decreased (4%), which implies that dissolution was dominant at first and then precipitation became much stronger after temperature increased (d_{306}). On the other hand, the porosity of S4 did not change much after the first imaging time, d_{119}. The porosity of S4 before reaction is expected to be similar as that of S3 before reaction because same sand was packed. Therefore, this graph indicates that the porosity of S4 first increased as S3 and then did not change much after d_{119}.

As shown in Figure 18, sample S3 was well-registered but there was grain movement due to the dissolution. The rough grain boundary in d_{344} and d_{420} was generated by precipitation. Because of grain movement, only statistical analysis was performed; another samples, H_{pre} and

H_{dis}, had little grain movement, which made it possible to perform voxel-by-voxel analysis (§4.2).

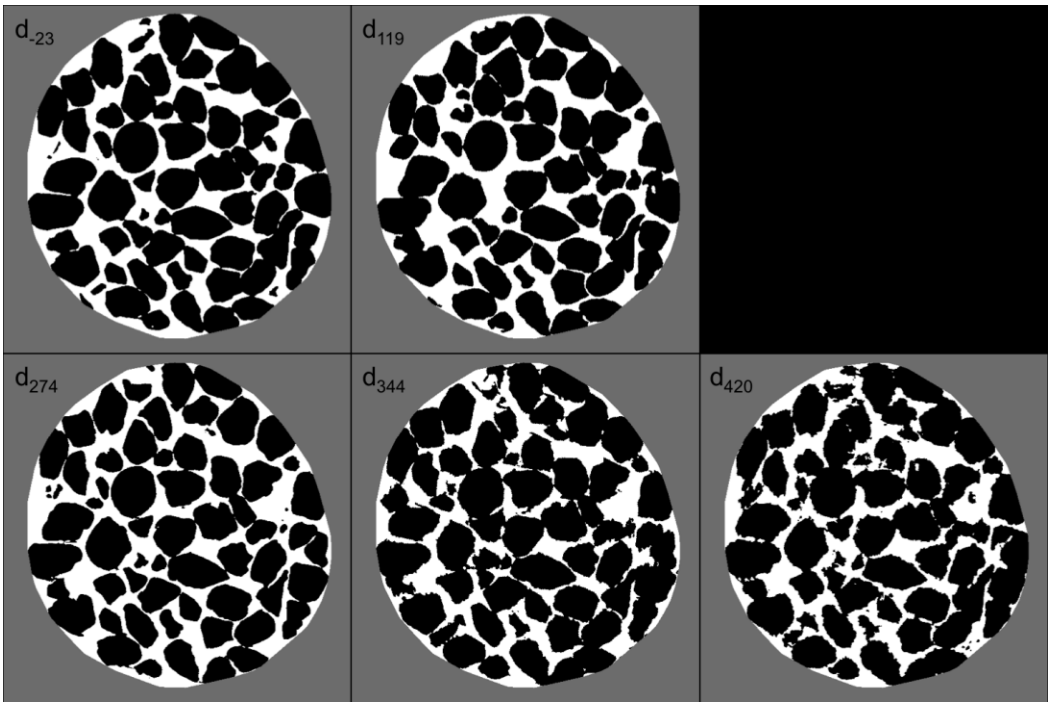

Figure 18. Segmented slice images of sample S3 section 3 after registration. White is void, black is grain.

The sequential injection of STWL into sample S3 resulted in significant changes in pore throat networks (Figure 19 and Figure 20). While the pore volume and throat area distributions of sample S4 did not change over time, those of sample S3 dramatically changed after temperature increased; strong precipitation decreased large pores' volumes and produced many small pores (Figure 19). The similar behavior was also observed on throat area distributions (Figure 20).

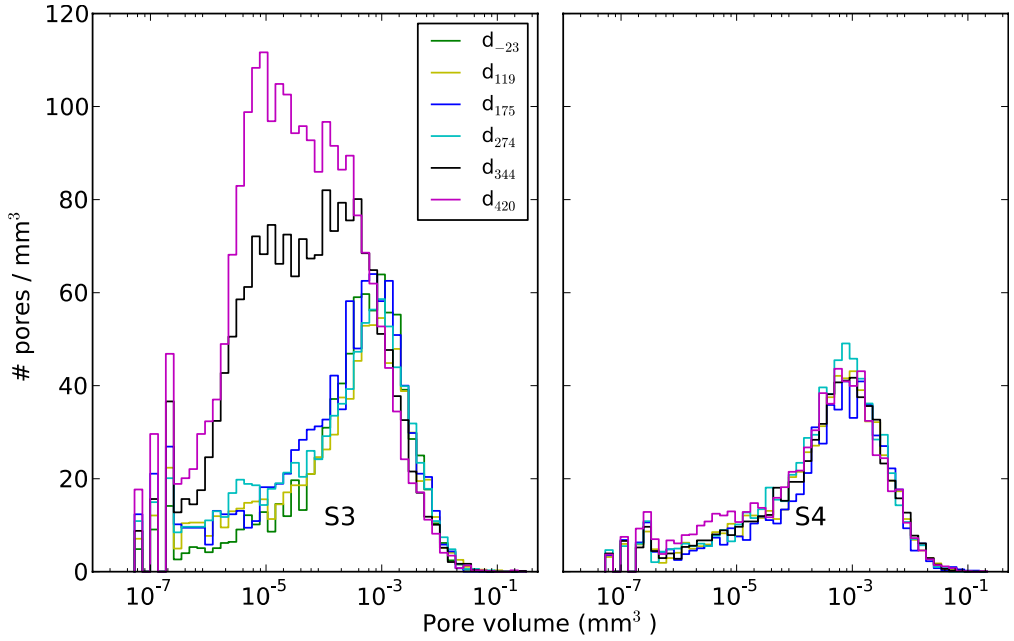

Figure 19. Pore volume distribution of sample S3 and S4.

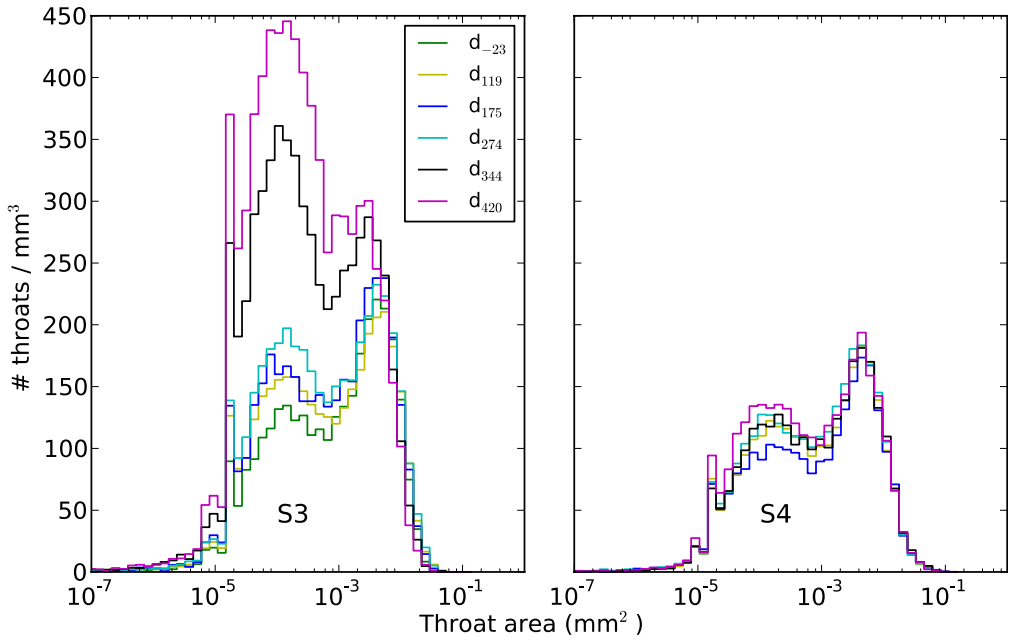

Figure 20. Throat area distribution of sample S3 and S4.

4.2. Hanford Sample

4.2.1. XCMT image

Figure 21 shows a 6.78 mm × 7.66 mm region from a single slice of the Sec1 images of H_{pre}. The t_0 image indicates that XCMT distinguishes roughly two classes of sediment grains, greyish grains (lower CT value) and black grains (higher CT value). For brevity, we refer to these two grain classes as G1 and G2. Five grains are labeled in the Figure 21, one black (grain 1) and four grey (grains 2 to 5). Effects of apparent dissolution and precipitation are visible in the t_{90} and t_{241} images. The black grains appear largely unaffected by the reactive processes. The grey grains exhibit a large variation of effect: grain 3 appears unaffected while grain 2 appears to dissolve completely with its outline preserved by what appears to be precipitated material. Grains 4 and 5 show "intermediate stages" of dissolution. It is a reasonable assumption that a combination of two factors causes the variation in behavior seen in the grey grains: i) such grains belong to different mineral types but show similar X-ray contrast and ii) grains may be of the same mineral type but have varied initial intra-particle porosity. The dissolution behavior in grains such as 4 and 5 indicates that ii appears to be a factor. These factors are addressed in the SEM studies discussed below. Three dimensional characterization of the geometrical changes observed is addressed by full 3D image analysis.

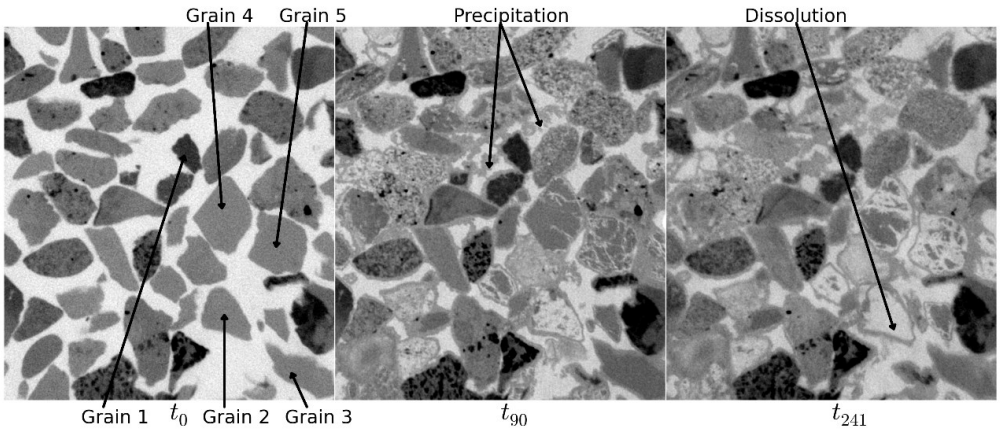

Figure 21. Detail of a single slice of successive XCMT images of Sec1 for column H_{pre}. Darker colors represent increasing X-ray absorption (higher CT value).

4.2.2. Image correction

The reconstructed images obtained from PNNL consisted of CT values in floating point format with the majority of the CT signal lying in the range (0.0, 200.0). As the 3DMA-Rock software package used for the analysis performs some fundamental analyses in integer arithmetic, the initial data was converted to integer values by scaling first by a factor of 256 to preserve dynamic range.

Initial review of the images indicated two artifacts. Images near the Sec1 of both columns extended into the end-cap, reducing the range of slices available for analysis. The analyzed region of each of the three images for H_{pre} covered $1700 \times 1700 \times 1000$ voxels ($19.2 \times 19.2 \times 11.3$ mm^3). For H_{dis}, the analyzed regions measured: Sec1 - $1678 \times 1678 \times 645$ ($19.0 \times 19.0 \times 7.3$ mm^3); Sec2 and Sec3 - $1678 \times 1678 \times 1000$ ($19.0 \times 19.0 \times 11.3$ mm^3).

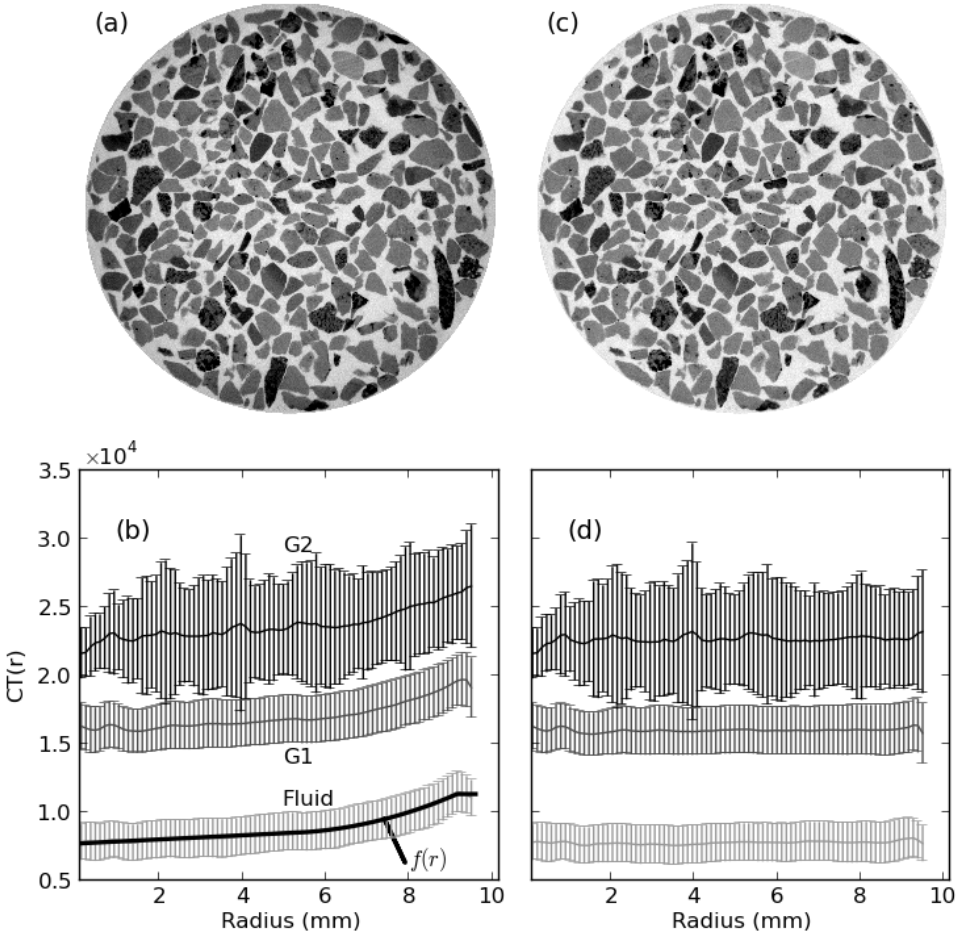

Figure 22. (a) A slice from the initially segmented t_0 image of the Sec1 of H_{pre}. (b) Plots of average CT value of the entire image $CT(r)$ (solid line) and standard deviation in CT value (error bars) as a function of radius from the tomographic axis of rotation of the image for the entire image of the Sec1. Plots are shown for the liquid phase, and the two CT-value distinct grain phases G1 and G2. The fitting curve $f(r)$ is superimposed upon $CT(r)$ for the liquid phase. (c) The slice in (a) after the subtraction $f(r) - f(0)$ was performed on the CT value in each voxel in the image. (d) Plots of the CT distributions after image correction.

More critically, all images contained a radial artifact in which the CT intensity in a single phase (as determined through initial segmentation) varied radially from the center of the sample. This radial variation was effectively constant among all images and was corrected as follows. Let $DT(r)$ denote the distribution of CT values at radius r (measured from the tomographic center of

rotation in each slice) in the liquid phase. Let $CT(r)$ denote the average value of this distribution as a function of r. The average, $CT(r)$, and standard deviations are plotted in Figure 22b for the t_0 Sec1 image of H_{pre}. Similar plots are shown for the other two phases (GP and DP). $CT(r)$ for the liquid phase was fit to the functional form

$$f(r) = \begin{cases} b_1 r + c_1, & 0 \le r \le 5.3 \text{ mm}, \\ a_2 r^2 + b_2 r + c_2, & 5.3 < r \le 9.2 \text{ mm}, \\ c_3, & r > 9.2 \text{ mm}. \end{cases} \quad (10)$$

The least squares fit to this form is also plotted in Figure 1d. The appropriate radial correction, $f(r) - f(0)$, was subtracted from the CT value of each voxel in the image. Since correction of CT values will affect segmentation (which in turn affects radial correction) this radial correction process was iterated four times on an image (until the segmentation stabilized). The functional fit for $f(r)$ used to correct the Sec1 image was also used to correct Sec2 and Sec3 images of H_{pre} at t_0. The values of the fitted parameters used for all images at each time point are presented in Table 2. Figure 22a and c show a single slice of the image before and after the radial correction is applied.

4.2.3. Image segmentation

In addition to the XCMT classification of mineral grains into two types, referred to here as G1 and G2, a gas phase is apparent in the t_{90} and t_{110} images of both columns, though interestingly not in the subsequent t_{241}, t_{261} images. We believe that the gas appears due to exsolution. Thus it seems that the gas phase is sufficiently mobile to flush though the column (or at least out of the field of view of the imaged sections). To capture these "phases", a four-phase segmentation was performed to identify the gas phase, the liquid phase, and two mineral "phases" as judged by X-ray contrast.

Table 2. Fits to radial correction $f(r)$ in fluid phase

			a_2 ($\times 10^2$)	b_1 ($\times 10^2$)	b_2 ($\times 10^3$)	c_1 ($\times 10^3$)	c_2 ($\times 10^4$)	c_3 ($\times 10^4$)
H_{pre}	t_0	Sec1	1.55(8)	1.50(7)	-1.5(1)	7.69(2)	1.21(4)	1.130(3)
		Sec2	1.54(8)	1.41(7)	-1.6(1)	7.49(2)	1.22(4)	1.080(3)
		Sec3	1.57(8)	1.47(6)	-1.5(1)	7.91(2)	1.25(4)	1.146(3)
	t_{90}	Sec1	1.84(19)	1.73(16)	-1.8(3)	9.13(5)	1.46(9)	1.320(7)
		Sec2	1.74(9)	2.80(7)	-1.8(1)	7.61(2)	1.37(4)	1.188(3)
		Sec3	1.33(24)	1.39(20)	-1.1(3)	7.84(7)	1.09(11)	1.159(9)
	t_{241}	Sec1	1.49(6)	1.74(5)	-1.3(1)	9.74(2)	1.35(3)	1.387(2)
		Sec2	1.59(6)	2.04(5)	-1.5(1)	9.74(2)	1.42(3)	1.397(3)
		Sec3	1.42(11)	2.02(9)	-1.3(2)	9.53(3)	1.35(5)	1.352(4)
H_{dis}	t_0	Sec1	1.12(11)	1.03(9)	-1.0(2)	6710(3)	0.93(5)	0.974(4)
		Sec2	1.27(9)	1.42(8)	-1.2(1)	6.53(3)	1.03(4)	0.958(4)
		Sec3	1.36(8)	1.52(7)	-1.4(1)	6.75(2)	1.09(4)	0.992(3)
	t_{110}	Sec1	1.58(15)	0.80(13)	-1.5(2)	8.70(4)	1.27(7)	1.207(6)
		Sec2	1.10(13)	0.76(11)	-1.0(2)	8.01(4)	1.04(6)	1.085(5)
		Sec3	1.70(15)	0.76(12)	-1.8(2)	7.78(4)	1.30(7)	1.068(6)
	t_{261}	Sec1	1.21(10)	1.40(8)	-1.0(1)	9.22(3)	1.18(5)	1.286(4)
		Sec2	1.41(7)	1.47(6)	-1.3(1)	9.35(2)	1.32(4)	1.282(3)
		Sec3	1.52(7)	1.96(6)	-1.5(1)	9.11(2)	1.37(3)	1.292(3)

Segmentation was performed using indicator-kriging[36] as stated in §2. In order to determine the threshold "window" values used by the indicator-kriging method, we utilized a Gaussian peak-fitting procedure illustrated in Figure 23. In Figure 23a, a Gaussian fit is first performed on the gas peak – identifying the CT values $\mu_g \pm \sigma_g$, where μ and σ are the respective mean and standard deviation from the peak fit. Subtraction of the gas peak gives the black curve in Figure 23b. Figure 23b shows the result of fitting the liquid phase peak, identifying the CT values $\mu_L \pm \sigma_L$. Figure 23c shows the result of fitting the resultant grain 1 peak, identifying the CT values $\mu_1 \pm \sigma_1$. Figure 23d shows the result of fitting the grain 2 peak, identifying the CT values $\mu_2 \pm \sigma_2$. With these threshold values identified, the 3D image is then segmented using the following bi-phase segmentations. On the entire image, a fluid-solid segmentation is performed

using the kriging window $[\mu_L + \sigma_L, \mu_1 - \sigma_1]$. Then a bi-phase segmentation is performed *only in the so-identified solid phase* using the kriging window $[\mu_1 + \sigma_1, \mu_2 - \sigma_2]$. This identifies the G1 and G2 mineral phases. Finally (in the $t_{90}$and t_{110} images) a bi-phase segmentation is performed only in the fluid phase using the kriging window $[\mu_g + \sigma_g, \mu_L - \sigma_L]$. This identifies the gas and liquid phases in the image.

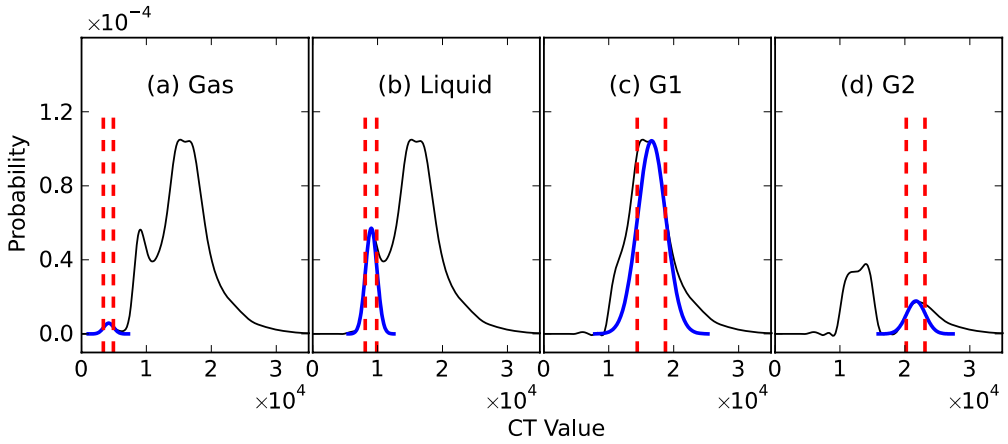

Figure 23. Gaussian peak-fitting procedure illustrated for the Sec1 image of H_{pre} at t_{90}. In (a) the black curve is the initial histogram; in (b), (c) and (d) the black curve is the cumulative, peak-subtracted histogram. Blue curves are Gaussian peak-fits.

4.2.4. Statistical analysis

With no Al in the STWL composition, we expect dissolution processes to dominate in column H_{dis} (though secondary precipitation could occur from dissolution of Al species within the pack of Hanford grains) while dissolution and precipitation processes both occur in H_{pre}. Figure 24(a) and (d) compare the (radially corrected) distributions of CT values for the Sec1, Sec2 and Sec3 images prior to reactive flow. The similarity of these distributions supports the

conclusion that each column was homogeneously packed along its length. Figure 24 (e) and (f) compare distributions along the column at time-points t_{110} and t_{261} in H_{dis}. The results are consistent with the observation of more dissolution occurring at the Sec1 of the column than at the Sec3. The effect is greater at t_{110} than at t_{261} suggesting that the dissolution is more uniform throughout the column after 261 days of reactive flow. Reactive flow differences along the column are more striking for column $H_{pre.}$ At t_{90} (Figure 24(b)) net-precipitation (precipitation minus dissolution) is more advanced at the Sec1 than at the Sec3. While Sec1 and Sec3 distributions appear similar at t_{241} (Figure 24(c)), the Sec2 distribution shows indication of greater net-precipitation.

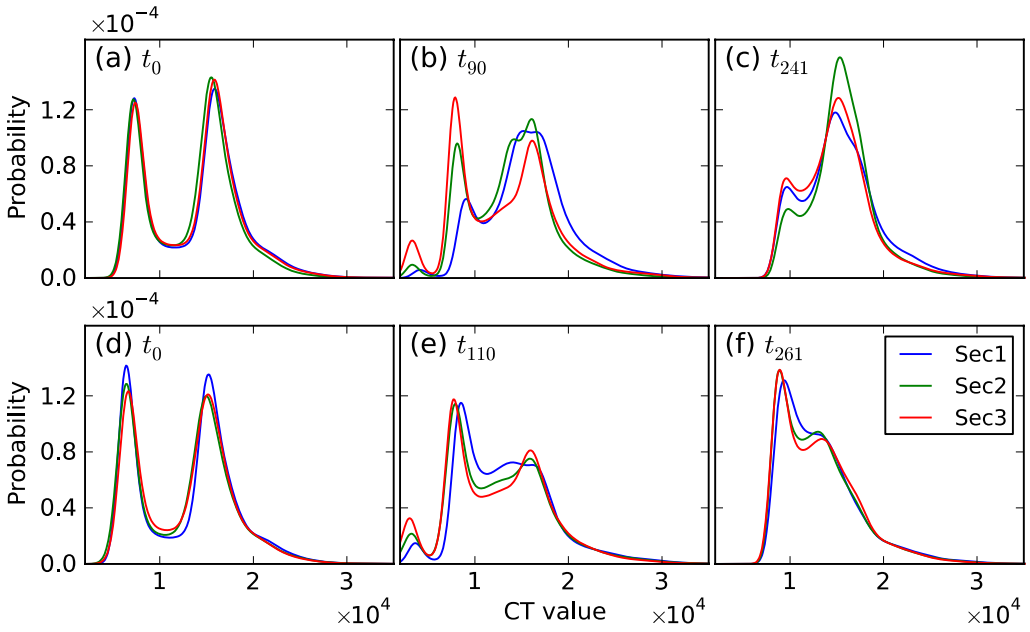

Figure 24. Comparison of CT value distributions along the column (Sec1, Sec2, Sec3) at the different time-points for (a), (b), (c) H_{pre} and (d), (e) (f) H_{dis}.

Gas bubbles clearly appear in all three sections of the column at the mid-time-point (t_{90} and t_{110}) of both flow columns. There is no evidence of gas at the earlier or later time-points. Table 3 gives the percent volume occupied by the gas phase in each section. Two trends are noticeable. The gas phase increases with distance downstream consistent with increased exsolution at lower (downstream) pore pressures and with downstream movement of gas bubbles. Intriguingly, the gas phase is several percent larger in H_{dis} than in H_{pre}.

Table 3. Phase occupation by volume (%).

		H_{pre}			H_{dis}		
		t_0	t_{90}	t_{241}	t_0	t_{110}	t_{261}
Sec1	Gas		1.43			4.09	
	Liquid	32.23	17.37	18.63	35.23	33.04	40.58
	G1	54.01	65.69	68.44	53.94	52.78	51.51
	G2	13.75	15.51	12.96	10.83	10.08	7.91
Sec2	Gas		2.01			5.81	
	Liquid	32.19	26.35	13.16	33.6	32.97	39.64
	G1	56.64	59.29	73.45	54.79	48.98	50.68
	G2	11.18	12.35	13.39	11.61	12.24	9.68
Sec3	Gas		5.33			7.67	
	Liquid	30.86	32.03	18.69	33.6	30.95	39.96
	G1	56.46	48.41	69.27	54.79	49.34	51.19
	G2	12.68	14.23	12.04	11.61	12.03	8.84

Changes in phase volumes for both columns are summarized graphically in Figure 25 from the data in Table 3. In Figure 25 the gas and liquid phases are combined to show the

porosity change. For column H_{dis}, the porosity increased with time at a similar rate throughout the column; on average the porosity changed by just under 6% over the 261 days of exposure to STWL flow. The G1 phase volume decreased, on average by 3.38% over 261 days, consistent with dissolution predominance. At the last time-point (261 days), the phase volume of phase G2 showed average changes of 2.81%, which may indicate later time dissolution or may possibly be due to segmentation errors affected by grain shifting.

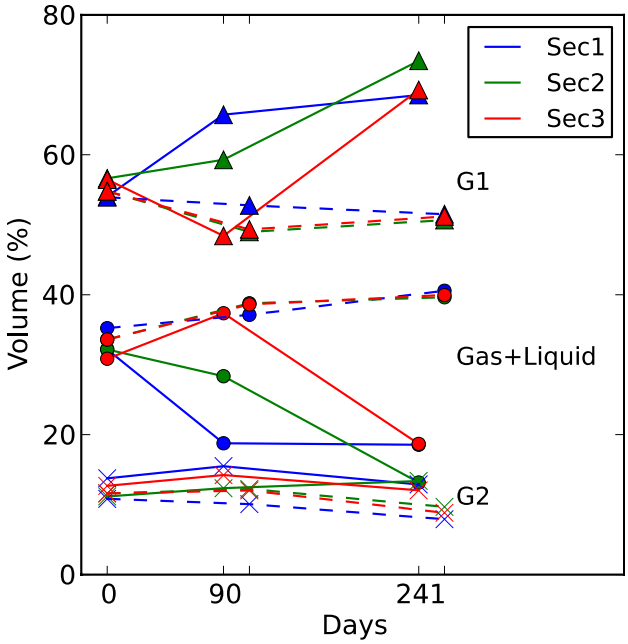

Figure 25. Phase volume changes. Solid lines are for H_{pre} and dashed lines are for H_{dis}.

Changes in H_{pre} are more pronounced, both in time and along the column. The porosity showing a marked decrease in volume fraction over 241 days (−13.6% Sec1; −19.0% Sec2; −12.2% Sec3). At t_{90} however, while the Sec1 and Sec2 showed the effects of net precipitation, the Sec3 showed effects of net dissolution (a +6.5% increase in porosity). By 241 days, the

porosity of the Sec3 fell by −16.7% showing that precipitation effects dominated there as well. Consistent with this, the G1 phase showed a marked increase in volume (+14.4% Sec1; +16.8% Sec2; +12.8% Sec3). At t_{90}, consistent with the Sec3 showing net dissolution, the G1 phase volume fell by −8.0%. For H_{pre}, the average magnitude of change in the G2 phase fraction from one time-point to the next was 1.7%, slightly smaller than the average $t_{110} \rightarrow t_{261}$ change noted in H_{dis}. We are led to postulate that G2 grains may not shift as much in column H_{pre} due to the "packing" quality of the precipitate that forms.

4.2.5. Subtraction

It is tempting to subtract successive images to document local change. Doing so with accuracy requires precise registration of successive images and knowledge that there is no relative internal movement of components in the image. The first is significant considering that images of the column were taken at widely spaced times and the columns had to be physically moved from flow laboratory to the XCMT system. The second is significant due to the dissolution and precipitation processes taking place. In particular, in H_{dis} where no significant precipitation is expected to occur, grain dissolution can lead to loss of contact support and grain movement in the liquid flow field.

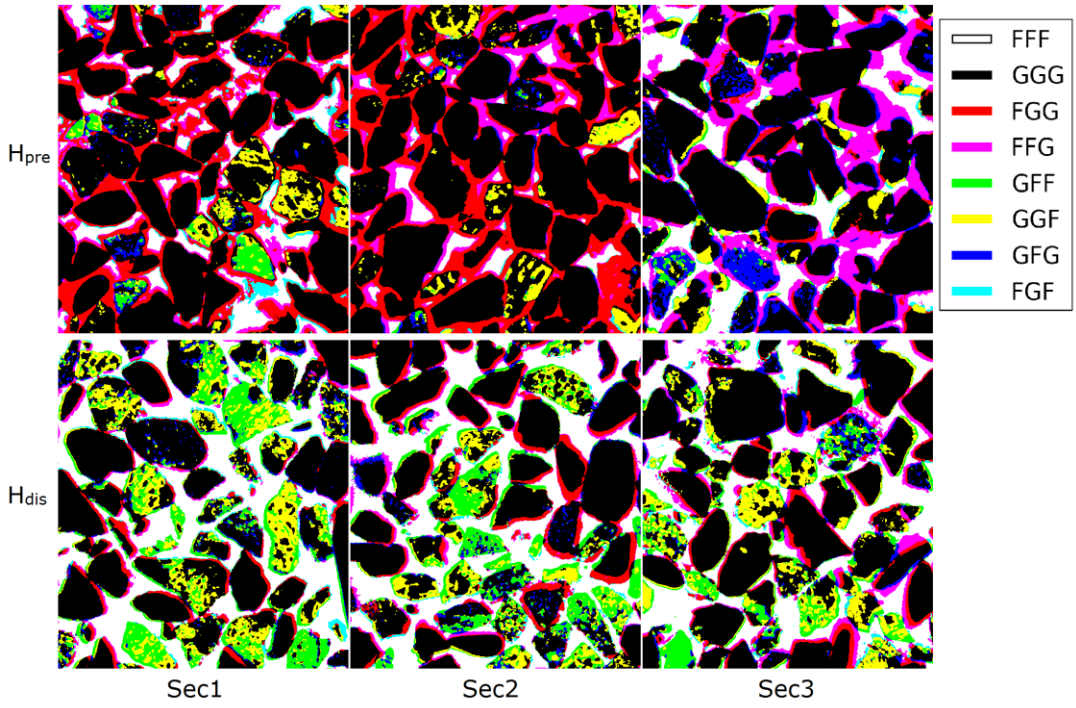

Figure 26. Summary of reactive changes seen in 6.78 mm × 7.66 mm subregions of three slices taken from the Sec1, Sec2 and Sec3 images of H_{pre} and H_{dis}. Each color corresponds to a three digit time-sequence label. The first digit refers to the phase identification at t_0; the second digit to phase identification at time t_{90}; and the last to time t_{241}. The phases are lumped: the digit G refers to grain phase (either G1 or G2); F refers to fluid phase (either gas or liquid). Thus yellow voxels (GGF) are voxels that are identified as grain phase at times t_0, and t_{90} but are identified as fluid phase at t_{241}.

With successive time-points of the same image registered, voxel-by-voxel phase changes were recorded. In order to distinguish between intra-grain dissolution and grain external surface dissolution, we applied the following simple criteria. Let S_{t_1} and S_{t_2} denote segmented images of the same region at time-points t_1 and t_2, where $t_2 > t_1$. A fluid voxel, v_2, in S_{t_2} indicated a dissolution site if the corresponding voxel, v_1, in S_{t_1} was grain. If v_1 was completely surrounded by grain voxels, then v_2 was a site of intra-grain dissolution; otherwise, v_2 was a site of surface dissolution. Analogously, a grain voxel, v_2, was designated as a site of precipitation if the

corresponding v_1 was a fluid voxel. Generally $t_1 = t_0$ corresponding to the initial (unreacted) image.

To quantify depth of dissolution, we determined distances from each dissolution site voxel to the original (t_0) surface of the affected grain. Depth of precipitation was measured similarly. In both cases the distance was measured to the closest grain surface.

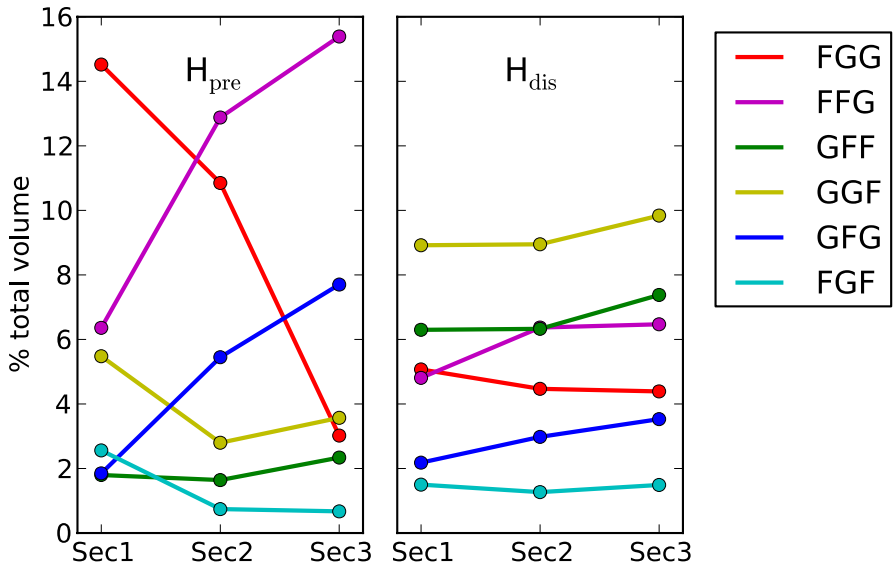

Figure 27. Quantitative summary of reactive changes by section. Color coding is as in Figure 26.

The reactive changes quantified in Figure 25 do not distinguish between inter-grain and intra-grain events. Figure 26 summarizes individual voxel history in 6.78 mm × 7.66 mm subregions of three slices taken from the Sec1, Sec2 and Sec3 images of H_{pre} and H_{dis}. (The Sec1 picture for H_{pre} in Figure 26 is, in fact, a summary of the changes displayed in Figure 21) Red and magenta colored voxels indicate precipitation occurring in regions that were fluid at t_0. Green and yellow voxels indicate dissolution occurring in regions that were grain at t_0. Dark

blue voxels can be interpreted as regions of dissolution at t_{90} followed by secondary precipitation at t_{241}. Red and magenta predominantly capture inter-grain processes while yellow, green and dark blue highlight intra-grain processes. The chosen sub-regions illustrated in the figure suggest that precipitation processes occurred earlier (red) in the Sec1 and later (magenta) towards the Sec3. Dissolution (yellow and green) processes appeared more commonly in the Sec1 and Sec2 and less commonly in the Sec3, with dissolution (green) occurring earlier at the Sec1 than in Sec2. In contrast, dark blue processes were more common at the Sec3.

Figure 27 quantifies these observations using data from entire images. In H_{pre}, inter-grain precipitation occurred earlier (FGG) in the Sec1, later (FFG) in the Sec3; intra-grain dissolution occurred more predominantly after t_{90} (GGF) rather than before (GFF). There is a strong signal that intra-grain dissolution followed by re-precipitation (GFG) occurred more predominantly downstream in the flow. In H_{dis} these inter- and intra-grain processes occurred much more uniformly along the length of the column. Dissolution processes (GFF, GGF) dominate with more dissolution occurring after t_{110} (GGF) than before (GFF). Precipitation processes (FGG, FFG) are also identified at a lower level of activity, with more precipitation occurring after t_{110} (FFG) than before (FGG).

Data in Figure 27 are presented as percent of total volume. The data are re-summarized in Table 4 in terms of percent of initial fluid (inter-grain space) and grain (intra-grain space) volume, as appropriate. The data indicate that, for H_{pre}, the imaging captures a dissolution "front" moving downstream producing upstream/downstream differences in the t_{90} image. By t_{241}this dissolution wave has effectively moved through the column and reactive results are more uniform along the column. Interestingly, in H_{dis} no such wave is visible, results remain more uniform along the column.

Table 4. Summary of inter- and intra-grain processes as percentage of t_0 fluid/grain space (as appropriate)

	H_{pre}		
	Sec1	Sec2	Sec3
Inter-grain space occupied by precipitate at time			
t_{90} (FGG)	45.1	33.6	9.8
t_{241} (FFG)	19.7	40.0	49.8
Inter-grain space precipitated at t_{90} re-dissolved at t_{240} (FGF)	7.9	2.3	2.2
Intra-grain space dissolution at time			
t_{90} (GFF)	2.7	2.4	3.4
t_{241} (GGF)	8.1	4.1	5.2
Intra-grain space dissolution at t_{90} re-precipitated at t_{240} (GFG)	2.7	8.0	11.1

	H_{dis}		
	Sec1	Sec2	Sec3
Inter-grain space occupied by precipitate at time			
t_{90} (FGG)	14.4	12.7	13.1
t_{241} (FFG)	13.7	18.1	19.3
Inter-grain space precipitated at t_{90} re-dissolved at t_{240} (FGF)	4.3	3.6	4.4
Intra-grain space dissolution at time			
t_{90} (GFF)	9.7	9.8	11.1
t_{241} (GGF)	13.8	13.8	14.8
Intra-grain space dissolution at t_{90} re-precipitated at t_{240} (GFG)	3.4	4.6	5.3

In H_{pre}, by t_{90}, Table 4 indicates (row FGG) that 45.1% of the original fluid space in the Sec1 has been occupied by precipitate; this falls to only 9.8% at the Sec3. However, by t_{241}, totals (sums of rows FGG + FFG) of 64.8% (Sec1), 73.6% (Sec2), and 59.6% (Sec3) of the original fluid space had been replaced by precipitate. In contrast, in H_{dis}, final totals of 28.1% (Sec1), 30.8% (Sec2) and 32.4% (Sec3) of the original fluid space were replaced by precipitate.

Thus the presence of Al ions in the STWL solution roughly doubled the precipitation in the pore space.

In H_{dis}, by t_{261}, Table 4 indicates (rows GFF + GGF) that totals of 23.5% (Sec1), 23.6% (Sec2) and 25.9% (Sec3) of the original grain space had dissolved. In contrast, in H_{pre}, by t_{241}, only 10.8% (Sec1), 6.5% (Sec2) and 8.6% (Sec3) of the original grain space showed dissolution effects. We are led to conclude that the presence of Al ions in the STWL solution caused secondary precipitation to re-occupy 60% to 70% of the grain space that dissolved. Table 1 documents direct evidence (rows GFG) for grain dissolution followed by precipitation in both columns.

Table 4 also documents evidence (rows FGF) that secondary precipitate re-dissolved.

To document the width of the precipitation layers that cover grains as well as the depth of dissolution into grains, we computed depth profiles using the L_∞ measure (in physical units of μm. Let $N_f(d)$ denote the number of fluid voxels at t_0 having distance measure d. Let $N_p(t;d)$ denote the number of fluid voxels having distance measure d that convert to grain phase at time t. ($N_p(0;d) = 0$.) Define the precipitation ratio $r_t^p = N_p(t;d)\ /N_f(11.3)$. Similarly, let $N_g(d)$ denote the number of grain voxels having distance measure d and $N_d(t;d)$ denote the number of grain voxels having distance measure d that convert to fluid phase at time t. Define the dissolution ratio $r_t^d = N_d(t;d)\ /N_g(11.3)$.

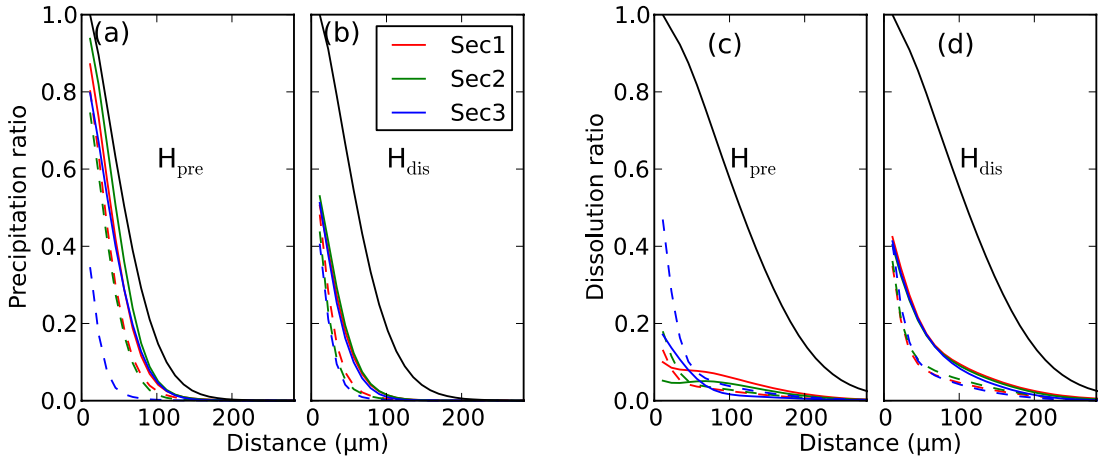

Figure 28. Precipitation depth profiles for (a) H_{pre}, (b) H_{dis}; dissolution depth profiles for (c) H_{pre}, (d) H_{dis}. Dashed lines represent the appropriate precipitation or dissolution ratios $r_{t_{90}}$ (H_{pre}) and $r_{t_{110}}$ (H_{dis}); solid lines represent the ratios $r_{t_{241}}$ (H_{pre}) and $r_{t_{261}}$ (H_{dis}). For comparison, the black lines represent normalized numbers of (a), (b) fluid $N_f(d)\ /N_f(11.3)$ and (c), (d) grain voxels $N_g(d)\ /N_g(11.3)$ as a function of distance d.

Figure 28 displays the measured profiles of r_t^p and r_t^d for the Sec1, Sec2 and Sec3 images. Except at the Sec3, by t_{90} over 80% of the distance 11.3 μm (first layer) of fluid voxels had precipitated in column H_{pre} (Figure 28(a)). For the Sec3 at t_{90} only 35% of distance 11.3 fluid voxels had precipitated. By t_{241} this had risen to 80%. The precipitation ratio drops with distance; no significant precipitation coated grains at a distance greater than 113 μm (layer 10). The observed precipitation behavior in column H_{dis} was smaller (Figure 28(b)); no more than 50% of distance 11.3 fluid voxels ever precipitated; no significant precipitation coated grains at a distance greater than 113 μm (layer 10) *which is consistent with intra-grain distances*. (In these images, 99% of void space lies within a 136 μm (12 voxel layers) distance of a grain surface.) Unlike H_{pre}, the precipitation depth profiles for H_{dis} showed uniformity at t_{90} and t_{110}. Dissolution depth profiles for H_{dis} (Figure 28(d)) also display uniformity at t_{90} and t_{110}. Fewer than 45% of distance 11.3 (layer 1) grain voxels ever dissolve, but dissolution depth into grains

proceeds to a depth of 226 μm (layer 20) – *consistent with grain size*. (In these images, 99% of grain space lies within 215 μm (19 voxel layers) of a grain surface.) Dissolution depth profiles for H_{pre} Figure 28(c)) display a more complex behavior with depth and with column position. At t_{90} Sec3 precipitation and dissolution profiles for H_{pre} are similar to those of H_{dis} Sec3, reinforcing, once again, that at t_{90}, the Sec3 is dissolution dominated. However, for the Sec2 and Sec1, as well as for all sections at t_{241}, the dissolution profile for H_{pre} is much reduced, reinforcing the conclusion that we have observed changes induced from secondary precipitation in intra-grain dissolved regions. Note that for all sections of the column for H_{pre}, $r_{241}^{d} < r_{90}^{d}$ for a small range of $d \geq 11.3\ \mu$m, indicating that grain surface voxels dissolved at t_{90} precipitated by t_{241}.

Table 5. Disconnected pore and grain volumes ignored in pore-network analysis

	H_{pre}			H_{dis}		
	t_0	t_{90}	t_{241}	t_0	t_{110}	t_{261}
	Disconn. Pore vol. %					
Sec1	0.005	1.339	2.452	0.006	0.147	0.108
Sec2	0.004	0.610	3.733	0.006	0.159	0.115
Sec3	0.005	0.121	1.582	0.005	0.100	0.094
	Disconn. Grain vol. %					
Sec1	0.000	0.023	0.089	0.000	0.059	0.141
Sec2	0.000	0.046	0.041	0.000	0.068	0.134
Sec3	0.000	0.090	0.007	0.000	0.079	0.226

4.2.6. Pore network

A common sample size was ensured by performing this analysis on a $1000 \times 1000 \times 1000$ voxel (11.3^3 mm^3) subvolume from each image (with the exception of the Sec1 region of H_{dis} where the $1000 \times 1000 \times 645$ voxel image was analyzed).

Table 5 documents the volume of pore voxels so-converted in each image. The occurrence grows with time, indicating the increased complexity of the pore network as dissolution and precipitation processes continue.

In the worst case (Sec2 image at t_{241}), 3.7% of the volume consisted of such disconnected pore space. Given the limitation of the voxel size, XCMT provides no means to determine how accessible this pore space is to fluid flow, though we suspect it probably is. Figure 29 documents the distribution (number per unit volume) of these disconnected voids and grains as a function of their perceived volume under XCMT. Note that these pore volumes are not included in the pore volume distributions presented in Figure 30. In the worst case, (Sec3 image at t_{261}), a negligible 0.23% of the grain space appeared disconnected – ignoring it should produce negligible effect of the pore-network analysis.

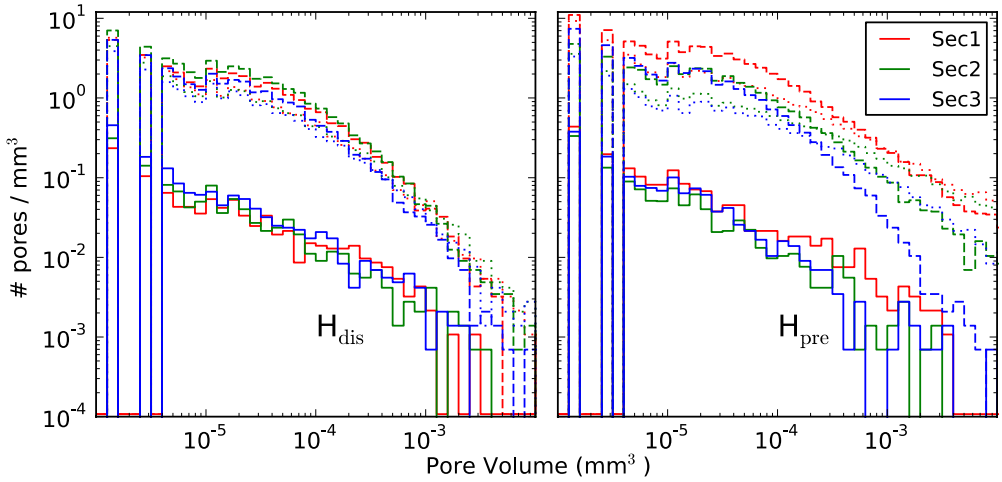

Figure 29. Comparison of distributions of disconnected intra-grain pore volumes observed in H_{dis} at: t_0 (solid line), t_{110} (dashed line) and t_{261} (dotted line) and in H_{pre} at: t_0 (solid), t_{90} (dashed) and t_{241} (dotted).

Pore volume distributions from the pore-throat network analysis are presented in Figure 30. In order to best compare between images (both spatially and in time) we normalize the distributions by plotting number of pores/unit-volume as a function of pore volume. Once again we see uniformity of behavior of the images along the column (Sec1, Sec2, Sec3) as a function of time. There is a decrease in the density of large pores (volume larger than $2 \cdot 10^{-2}$ mm^3) with time – consistent with secondary precipitation. By t_{110} there is a striking increase in the density of pores with volume below 10^{-2} mm^3 consistent with intra-grain dissolution. By t_{261} there is a decrease in the density of these smaller sized pores, consistent with further intra-grain dissolution "merging" small intra-grain porosities.

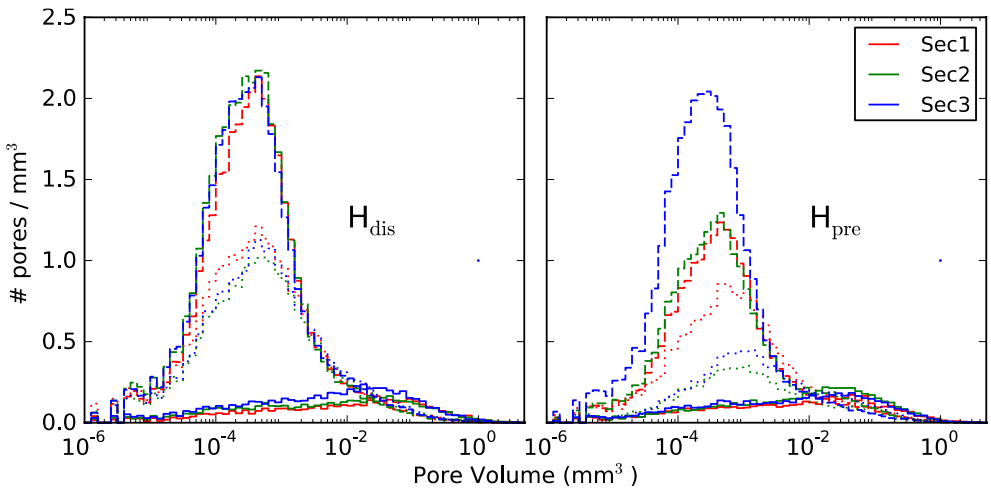

Figure 30. Comparison of pore volume distributions at H_{dis}: t_0 (solid line), t_{110} (dashed line) and t_{261} (dotted line) and H_{pre}: t_0 (solid), t_{90} (dashed) and t_{241} (dotted).

Pore volume distributions for H_{pre} are more differentiated, in time and in position along the column. Again there is a decrease in the density of large pore (volume larger than $2 \cdot 10^{-2}$

mm^3) with time – consistent with secondary precipitation. By t_{90} there is a striking increase in the density of pores with volume below 10^{-2} mm^3 in the Sec3 image consistent with the view that at this time the Sec3 is still dissolution dominated. However at t_{90} the distribution in this volume range in the Sec2 and Sec1 is already reduced, presumably due to intra-grain precipitation. By t_{241} there is a further decrease in the density of these smaller sized pores, consistent with intra-grain precipitation. Interestingly, at t_{241} the Sec1 still shows a large density of small sized pores indicating perhaps a continued "balance" between dissolution and precipitation processes. Throat density distributions as a function of throat area were also measured (Figure 31). The behavior of these distributions essentially duplicates that of the pore volume distributions.

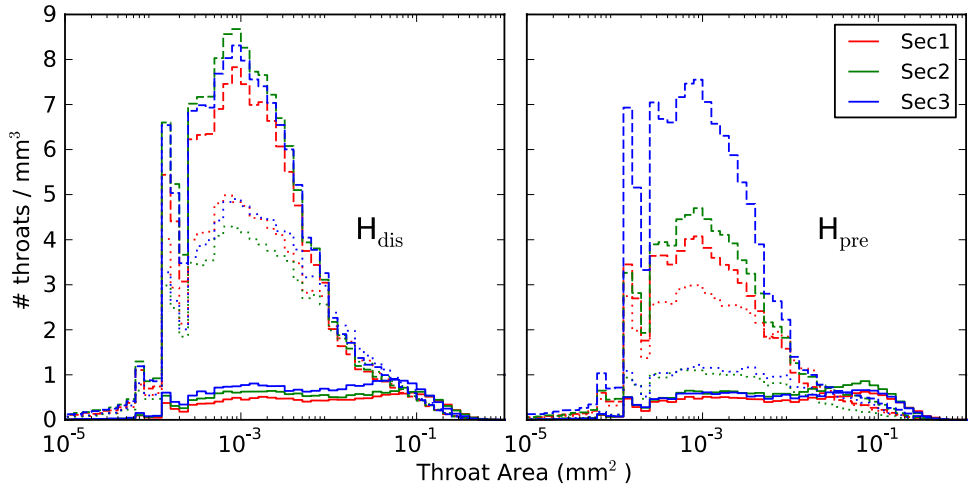

Figure 31. Comparison of throat area distributions at H_{dis}: t_0 (solid line), t_{110} (dashed line) and t_{261} (dotted line) and H_{pre}: t_0 (solid), t_{90} (dashed) and t_{241} (dotted).

Chapter 5

Discussion

One consequence of (the standard) definition, D1, for a throat is that entry menisci during drainage occur *in the downstream vicinity* of a throat; the deviation from throat location depends on wetting angle. In addition, depending on flow direction, no entry meniscus will occur at some throat locations. We have shown that throats so defined may intersect each other and propose a criterion (T5) for differentiating throats that do intersect. We have shown by numerical computation (§3) that these intersecting throats do indeed correspond to locations of capillary barriers to flow in intersecting directions.

A pore-network model is a standard construct used to visualize, simplify, and characterize the void space network in a porous medium, especially for the extremely random networks found in geologic media. The recognition that throat surfaces in such a network intersect each other, significantly so for porosities exceeding 20%, has implications for this construct. As throat surfaces approximate capillary barriers in drainage processes, one implication is that *drainage flow potentially bifurcates where throat surfaces intersect.* This has consequences (e.g. temporal order of wetting film formation) for network flow model computations.

The throat finding algorithm proposed here explicitly captures intersecting throats. In the interests of speed, throats are approximated as planar surfaces; it would be useful to have a fast algorithm to better approximate curved minimal-area surfaces. Our studies with this algorithm

indicate that the percentage of intersecting throats increases dramatically above 20% porosity. However, our high porosity sample is an unconsolidated sand pack, while our lower porosity samples are consolidated sandstones. We do not know how strongly the rate of throat intersection depends on consolidation of the grains.

Dissolution and precipitation by STWL changed the pore structure in the reactive experiment columns. Compared with the static column S4, the geometrical structure of sample S3 was changed by the reaction. The porosity of S3 increased (2%) during the first 274 days and decreased (4%) after temperature increased. The precipitation produced many small pores, which changed pore volume and throat area distributions. The observed grain movement limited our analysis; only statistical analysis was performed.

For Hanford sample H_{dis} images, based upon the three image time-points, t_0, t_{110} (55 pore volumes of STWL injected) and t_{261} (130.5 pore volumes of STWL injected), interpretation of the results for H_{dis} suggests that, in the absence of Al ions in the STWL, dissolution dominates (net increase of 4% porosity) secondary precipitation. Some precipitation is noted, suggesting the presence of native Al in the soil minerals. Geometrical changes were found to be relatively constant along the H_{dis} column at any given time-point. Roughly 25% of the original grain volume dissolved, with a notable component being intra-grain dissolution. Secondary precipitate formed in this column – filling about 30% of the original porosity, suggesting the presence of native Al in the soil minerals.

In contrast, even after injection of 45 pore volumes STWL (t_{90}), the H_{pre} column showed a decided reaction gradient, with the Sec3 dissolution dominated (+6.5% porosity increase), while the Sec2 (−3.8% porosity decrease) and Sec1 (−13.4% porosity decrease) sections were precipitation dominated. However, by t_{241}, (120.5 pore volumes STWL injected), the entire

length of column H_{pre} was precipitation dominated (−13.6% Sec1; −19.0% Sec2; −12.2% Sec3 porosity decreases). 60% to 75% of the original porosity was filled with secondary precipitate. A net 6% to 11% of the original grain volume showed evidence of dissolution at t_{241}. We estimate that ~25% of the original grain volume had dissolved (as for H_{dis}) and 60% to 75% of this dissolved volume then became occupied with secondary precipitate.

There was significant intra-grain dissolution and precipitation in Hanford samples. Visual and dissolution profile results indicate that some G1 grains were dissolved almost completely (e.g. grain 2 in Figure 21); their presence embodied by a shell of precipitate outlining the original grain boundary. With only limited time-point sampling, we appear to capture (Table 3) between 2.7% (Sec1) to 11.1% (Sec3) of the original grain space dissolving and then precipitating as cancrinite.

The significant amount of intra-grain dissolution produced a sharp rise in the number of smaller size pores (H_{dis}, Figure 30) which become somewhat ameliorated as dissolution continued to carve out larger intra-grain spaces. With secondary precipitation (H_{pre}, Figure 30) this amelioration occurs more rapidly presumably as precipitate begins to fill in these pores.

A significant question left un-addressed by our XCMT work is the identification of the minerals that comprise the G1 and G2 phases that we identify via CT contrast in our images. The highly attenuating G2 minerals are not appreciably dissolved though they do become coated with cancrinite precipitate (Figure 21). Most of the minerals of the G1 phase, which certainly contain the quartz grains, are involved in dissolution.

References

1 Macedo, A., Vaz, C. M. P., Naime, J. M., Cruvinel, P. E. & Crestana, S. X-ray microtomography to characterize the physical properties of soil and particulate systems. *Powder Technol.* 101, 178-182, doi:10.1016/s0032-5910(98)00170-3 (1999).

2 Coles, M. E. *et al.* Pore level imaging of fluid transport using synchrotron X-ray microtomography. *J. Petrol. Sci. Eng.* 19, 55-63, doi:10.1016/s0920-4105(97)00035-1 (1998).

3 Kinney, J. H. *et al.* X-ray Tomographic Study of Chemical Vapor Infiltration Processing of Ceramic Composites. *Science* 260, 789-792, doi:10.1126/science.260.5109.789 (1993).

4 Wildenschild, D., Vaz, C. M. P., Rivers, M. L., Rikard, D. & Christensen, B. S. B. Using X-ray computed tomography in hydrology: systems, resolutions, and limitations. *J. Hydrol.* 267, 285-297, doi:10.1016/s0022-1694(02)00157-9 (2002).

5 Nordbotten, J. M. Adaptive Variational Multiscale Methods for Multiphase Flow in Porous Media. *Multiscale Model. Simul.* 7, 1455-1473, doi:10.1137/080724745 (2009).

6 Andrew, M., Bijeljic, B. & Blunt, M. J. Pore-scale imaging of geological carbon dioxide storage under in situ conditions. *Geophysical Res. Lett.* 40, 3915-3918, doi:10.1002/grl.50771 (2013).

7 Cai, R., Lindquist, W. B., Um, W. & Jones, K. W. Tomographic analysis of reactive flow induced pore structure changes in column experiments. *Adv. Water Resourc.* 32, 1396-1403, doi:10.1016/j.advwatres.2009.06.006 (2009).

8 Kim, D., Peters, C. A. & Lindquist, W. B. Upscaling geochemical reaction rates accompanying acidic CO2-saturated brine flow in sandstone aquifers. *Water Resour. Res.* 47, doi:10.1029/2010wr009472 (2011).

9 Kim, D. & Lindquist, W. B. Effects of network dissolution changes on pore-to-core upscaled reaction rates for kaolinite and anorthite reactions under acidic conditions. *Water Resourc. Res.* 49, doi:10.1002/2013WR013667 (2013).

10 Bear, J. *Dynamics of Fluids in Porous Media*. (Dover, 1972).

11 Dullien, F. A. L. *Porous Media: Fluid Transport and Pore Structure*. (Academic Press, 1992).

12 Sholokova, Y., Kim, D. & Lindquist, W. B. Network flow modeling via lattice-Boltzmann based channel conductance. *Adv. Water Resour.* 32, 205-212 (2009).

13 Glantz, R. & Hilpert, M. Dual models of pore spaces. *Adv. Water Resourc.* 30, 227-248, doi:DOI 10.1016/j.advwatres.2005.11.017 (2007).

14 Lindquist, W. B. The geometry of primary drainage. *J. Colloid Interf. Sci.* 296, 655-668, doi:10.1016/j.jcis.2005.09.041 (2006).

15 Mayer, R. P. & Stowe, R. A. Mercury porosimetry-breakthrough pressure for penetration between packed spheres. *J. Colloid Interf. Sci.* 20, 893-911, doi:10.1016/0095-8522(65)90061-9 (1965).

16 Morrow, N. R. Physics and thermodynamics of capillary action in porous media. *Ind. Eng. Chem.* 62, 32-56, doi:Doi 10.1021/Ie50726a006 (1970).

17 Princen, H. M. Capillary phenomena in assemblies of parallel cylinders. I. Capillary rise between 2 cylinders. *J. Colloid Interf. Sci.* 30, 69-75, doi:10.1016/0021-9797(69)90379-8 (1969).

18 Frette, O. I. & Helland, J. O. A semi-analytical model for computation of capillary entry pressures and fluid configurations in uniformly-wet pore spaces from 2D rock images. *Adv. Water Resour.* 33, 846-866 (2010).

19 Blunt, M. J. Flow in porous media - pore-network models and multiphase flow. *Curr. Opin. Colloid Interf. Sci.* 6, 197-207 (2001).

20 Lindquist, W. B. & Venkatarangan, A. Investigating 3D geometry of porous media from high resolution images. *Phys. Chem. Earth (A)* 24, 593-599, doi:Doi 10.1016/S1464-1895(99)00085-X (1999).

21 Shin, H., Lindquist, W. B., Sahagian, D. L. & Song, S. R. Analysis of the vesicular structure of basalts. *Comput. Geosci.* 31, 473-487, doi:10.1016/j.cageo.2004.10.013 (2005).

22 Silin, D. & Patzek, T. Pore space morphology analysis using maximal inscribed spheres. *Physica A* 371, 336-360, doi:DOI 10.1016/j.physa.2006.04.048 (2006).

23 Glantz, R. & Hilpert, M. Tight dual models of pore spaces. *Adv. Water Resourc.* 31, 787-806, doi:10.1016/j.advwatres.2008.01.015 (2008).

24 Kim, J.-W., Kim, D. & Lindquist, W. B. A re-examination of throats. *Water Resour. Res.* 49, 7615-7626, doi:10.1002/2013wr014254 (2013).

25 Kim, J.-W., Wang, G., Beckingham, L., Um, W., Peters, C. & Lindquist, W. B. Inter- and intra-granular pore evolution in sediment via mineral dissolution and precipitation. *in progress*.

26 Bauer, A. & Berger, G. Kaolinite and smectite dissolution rate in high molar KOH solutions at 35 degrees and 80 degrees C. *Appl. Geochem.* 13, 905-916, doi:10.1016/s0883-2927(98)00018-3 (1998).

27 Brady, P. V. & Walther, J. V. Controls on silicate dissolution rates in neutrao and basic pH solutions at 25 °C. *Geochim. Cosmochim. Acta* 53, 2823-2830, doi:10.1016/0016-7037(89)90160-9 (1989).

28 Knauss, K. G. & Wolery, T. J. The dissolution kinetics of quartz as a funciton of pH and time at 70 °C. *Geochim. Cosmochim. Acta* 52, 43-53, doi:10.1016/0016-7037(88)90055-5 (1988).

29 Rimstidt, J. D. & Barnes, H. L. The kinetics of silica-water reactions. *Geochim. Cosmochim. Acta* 44, 1683-1699, doi:10.1016/0016-7037(80)90220-3 (1980).

30 Um, W. & Serne, R. J. Sorption and transport behavior of radionuclides in the proposed low-level radioactive waste disposal facility at the Hanford site, Washington. *Radiochimica Acta* 93, 57-63, doi:10.1524/ract.93.1.57.58295 (2005).

31 Wang, G. H. & Um, W. Mineral dissolution and secondary precipitation on quartz sand in simulated Hanford tank solutions affecting subsurface porosity. *Journal of Hydrology* 472, 159-168, doi:10.1016/j.jhydrol.2012.09.021 (2012).

32 Prodanovic, M., Lindquist, W. B. & Seright, R. S. Porous structure and fluid partitioning in polyethylene cores from 3D X-ray microtomographic imaging. *J. Colloid Interf. Sci.* 298, 282-297 (2006).

33 Zachara, J. M. *et al.* Geochemical processes controlling migration of tank waste in Hanford's vadose zone. *Vadose Zone J.* 6, 985-1003, doi:10.2136/vzj2006.0180 (2007).

34 Lindquist, W. B. *http://www.ams.sunysb.edu/~lindquis/3dma/3dma_rock/3dma_rock.html*.

35 Lee, T. C., Kashyap, R. L. & Chu, C. N. Building skeleton models via 3-D medial surface axis thinning algorithms. *CVGIP: Graphical Models Image Process.* 56, 462-478 (1994).

36 Oh, W. & Lindquist, W. B. Image thresholding by indicator kriging. *IEEE Trans. Pattern Anal. Mach. Intell.* 21, 590-602 (1999).

37 Prodanovic, M., Lindquist, W. B. & Seright, R. S. Porous structure and fluid partitioning in polyethylene cores from 3D X-ray microtomographic imaging. *J. Colloid Interf. Sci.* 298, 282-297, doi:10.1016/j.jcis.2005.11.053 (2006).

38 Lenormand, R., Zarcone, C. & Sarr, A. Mechanisms of the displacement of one fluid by another in a network of capillary ducts. *J. Fluid Mech.* 135, 337-353 (1983).

39 Joekar-Niasar, V., Hassanizadeh, S. M., Pyrak-Nolte, L. J. & Berentsen, C. Simulating drainage and imbibition experiments in a high-porosity micromodel using an unstructured pore network model. *Water Resourc. Res.* 45, W02430 (2009).

40 Koplik, J. & Lasseter, T. J. Two-phase flow in random network models of porous media. *Soc. Pet. Engin. J.* 25, 89-100 (1985).

41 van der Marck, S. C., Matsuura, T. & Glas, J. Viscous and capillary pressures during drainage: Network simulations and experiments. *Phys. Rev. E* 56, 5675-5687 (1997).

42 Raoof, A. & Hassanizadeh, S. M. A new formulation for pore-network modeling of two-phase flow. *Water Resourc. Res.* 48, W01514, doi:Doi 10.1029/2010wr010180 (2012).

43 Kovscek, A. R. & Radke, C. J. Gas bubble snap-off under pressure-driven flow in constricted noncircular capillaries. *Colloids Surf. A* 117, 55-76, doi:Doi 10.1016/0927-7757(96)03637-0 (1996).

44 Gao, S. Y., Meegoda, J. N. & Hu, L. M. Two methods for pore network of porous media. *Int. J. Num. Anal. Meth. Geomech.* 36, 1954-1970, doi:Doi 10.1002/Nag.1134 (2012).

45 Shaeri, M. R., Beyhaghi, S. & Pillai, K. M. On applying an external-flow driven mass transfer boundary condition to simulate drying from a pore-network model. *Int. J. Heat Mass Trans.* 57, 331-344, doi:DOI 10.1016/j.ijheatmasstransfer.2012.10.005 (2013).

46 Edelsbrunner, H. & Harer, J. in *Surveys on Discrete and Computational Geometry. Twenty Years Later* Vol. 453 (eds J.E. Goodman, J. Pach, & R. Pollack) 257-282 (American Mathematical Society, 2008).

47 Princen, H. M. Capillary phenomena in assemblies of parallel cylinders. 2. Capillary rise in systems with more than 2 cylinders. *J. Colloid Interf. Sci.* 30, 359-371, doi:10.1016/0021-9797(69)90403-2 (1969).

48 Hwang, S. K. The Gauss equation in capillarity. *Z. Phys. Chem.* 105, 225-235 (1977).

49 Prodanovic, M. & Bryant, S. L. A level set method for determining critical curvatures for drainage and imbibition. *J. Colloid Interf. Sci.* 304, 442-458, doi:10.1016/j.jcis.2006.08.048 (2006).

50 Lindquist, W. B., Venkatarangan, A., Dunsmuir, J. & Wong, T. F. Pore and throat size distributions measured from synchrotron X-ray tomographic images of Fontainebleau sandstones. *J. Geophys. Res.* 105, 21509-21527, doi:Doi 10.1029/2000jb900208 (2000).